J|A|C|S
ARTICLES

Published on Web 07/02/2008

n-Channel Polymers by Design: Optimizing the Interplay of Solubilizing Substituents, Crystal Packing, and Field-Effect Transistor Characteristics in Polymeric Bithiophene-Imide Semiconductors

Joseph A. Letizia, Michael R. Salata, Caitlin M. Tribout, Antonio Facchetti,* Mark A. Ratner,* and Tobin J. Marks*

Department of Chemistry and the Materials Research Center, Northwestern University, 2145 Sheridan Road, Evanston, Illinois 60208

Received December 4, 2007; E-mail: a-facchetti@northwestern.edu; ratner@northwestern.edu; t-marks@northwestern.edu

Abstract: Electron transporting (n-channel) polymer semiconductors for field-effect transistors are rare. In this investigation, the synthesis and characterization of new electron-depleted *N*-alkyl-2,2′-bithiophene-3,3′-dicarboximide-based π-conjugated homopolymers and copolymers containing the 2,2′-bithiophene unit are reported. A novel design approach is employed using computational modeling to identify favorable monomer properties such as core planarity, solubilizing substituent tailorability, and appropriate electron affinity with gratifying results. Monomeric model compounds are synthesized to confirm these properties, and a crystal structure reveals a short 3.43 Å $\pi-\pi$ stacking distance with favorable solubilizing substituent orientations. A family of 10 homopolymers and bithiophene copolymers is then synthesized via Yamamoto and Stille polymerizations, respectively. Two of these polymers are processable in common organic solvents: the homopolymer poly(*N*-(2-octyldodecyl)-2,2′-bithiophene-3,3′-dicarboximide) (**P1**) exhibits n-channel FET activity, and the copolymer poly(*N*-(2-octyldodecyl)-2,2′:5′,2″:5″,2‴-quaterthiophene-3,3′-dicarboximide) (**P2**) exhibits air-stable p-channel FET operation. After annealing, **P1** films exhibit a very high degree of crystallinity and an electron mobility $>$ 0.01 $cm^2\ V^{-1}\ s^{-1}$ with a current on−off ratio of 10^7, which is remarkably independent of film-deposition conditions. Extraordinarily, **P1** films also exhibit terracing in AFM images with a step height matching the X-ray diffraction *d* spacing, a rare phenomenon for polymeric organic semiconductors. Another fascinating property of these materials is the air-stable p-channel FET performance of annealed **P2** films, which exhibit a hole mobility of $\sim$0.01 $cm^2\ V^{-1}\ s^{-1}$ and a current on−off ratio of 10^7.

Introduction

Interest in organic electronics is inspired by the promise of low-cost printed electronics and the significant scientific challenges that must be overcome for this goal to be realized. Potential applications enabled by the lower-cost processing methods and unique mechanical properties of organics include lightweight flexible displays, RFID tags, and sensors.[1,2] Many of these applications demand dielectrics, conductors, and semiconductors that are solution-processable under ambient conditions using conventional printing techniques.[3–13] In addition to these processability requirements, important fundamental questions remain about long-range charge transport in organic solids, especially for polymeric semiconductors used in field-effect transistors (FETs).

Recent studies have demonstrated robust, air-stable performance in p-channel FETs using thiophene-based polymeric

(1) Bao, Z. R.; Katz, J. A.; Howard, E. *J. Mater. Chem.* **1999**, *9*, 1895–1904.
(2) (a) *Low Molecular Weight Organic Semiconductors*; Kampen, T. U., Ed.; Wiley-VCH: Weinheim, 2007. (b) *Conducting Organic Materials and Devices*; Jain, S. C., ; Willander, M., ; Kumar, V., Eds.; Elsevier Science: New York, 2007; Vol. 81, p 196. (c) Salleo, A. *Mater Today* **2007**, *10*, 38–45. (d) *Organic Electronics*; Klauk, H., Ed.; Wiley-VCH: Weinheim, 2006; p 428. (e) De Leeuw, D. M.; et al. *Nat. Mater.* **2004**, *3*, 106–110. (f) Kelley, T. W.; Baude, P. F.; Gerlach, C.; Ender, D. E.; Muyres, D.; Haase, M. A.; Vogel, D. E.; Theiss, S. D. *Chem. Mater.* **2004**, *16*, 4413–4422. (g) Dimitrakopoulos, C. D.; Malefant, R. L. *Adv. Mater.* **2002**, *14*, 99–117. (h) *Printed Organic and Molecular Electronics*; Gamota, D. R., ; Brazis, P., ; Kalyanasundaram, K., ; Zhang, J., Eds.; Springer: New York, 2004; p 720. (i) Fix, W.;; Ullmann, A.;; Ficker, J.;; Clemens, W. *Appl. Phys. Lett.* **2002**, *81*, 1735–1737. (j) Gelinck, G. H.; Geuns, T. C. T.; de Leeuw, D. M. *Appl. Phys. Lett.* **2000**, *77*, 1487–1489. (k) *Handbook of Oligo- and Polythiophenes*; Fichou, D., Ed.; Wiley-VCH: Weinheim, 1999. (l) Skotheim, T. A.; Elsenbaumer, R. L.; Reynolds, J. R. *Handbook of Conductive Polymers*; Marcel Dekker: New York, 1998.
(3) Pron, A. R. P. *Prog. Polym. Sci.* **2001**, *27*, 135–190.
(4) Sze, S. M. *Semiconductor Devices: Physics and Technology*; John Wieley & Sons, Inc.: New York, 2002.
(5) Bao, Z. N. *Nat. Mater.* **2004**, *3*, 137–138.
(6) Chabinyc, M. L.; Salleo, A. *Chem. Mater.* **2004**, *16*, 4509–4521.
(7) Forrest, S. R. *Nature* **2004**, *428*, 911–918.
(8) Kawase, T.; Sirringhaus, H.; Friend, R. H.; Shimoda, T. *Adv. Mater.* **2001**, *13*, 1601–1606.
(9) Knobloch, A.; Manuelli, A.; Bernds, A.; Clemens, W. *J. Appl. Phys.* **2004**, *96*, 2286–2291.
(10) Meijer, E. J.; De Leeuw, D. M.; Setayesh, S.; Van Veenendaal, E.; Huisman, B. H.; Blom, P. W. M.; Hummelen, J. C.; Scherf, U.; Klapwijk, T. M. *Nat. Mater.* **2003**, *2*, 678–682.
(11) Sirringhaus, H.; Kawase, T.; Friend, R. H.; Shimoda, T.; Inbasekaran, M.; Wu, W.; Woo, E. P. *Science* **2000**, *290*, 2123–2126.
(12) Hadziioannou, G.; Malliaras, G. G. *Semiconducting Polymers*; Wiley-VCH: New York, 2006; p 743.
(13) Bao, Z. *Adv. Mater.* **2000**, *12*, 227–230.

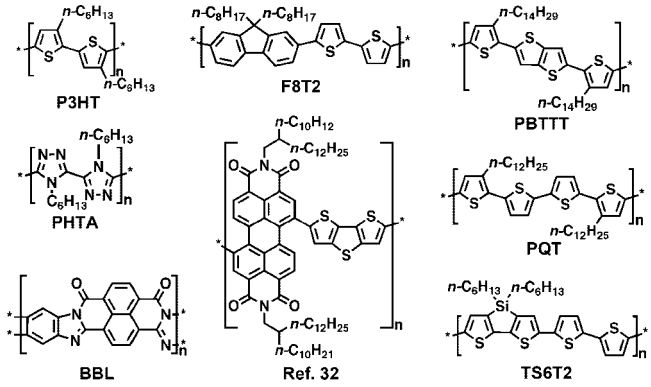

Figure 1. Representative semiconducting polymers.

semiconductors (Figure 1).[14–22] Unfortunately, there is a lack of polymeric semiconductors with comparable processing and performance characteristics for n-channel FETs. This is important since both hole (p-type) and electron (n-type) materials and devices are required to achieve low-power consumption complementary organic circuitry (CMOS).[23–25] In addition to such logic and switching applications, polymers exhibiting efficient electron transport and high electron affinities should also be useful as acceptor materials in organic photovoltaics and as electron-transporting materials in polymer-based light-emitting diodes.[26–29]

Limited progress has been made in developing polymer-based n-channel FETs. The first report of an n-channel FET-active polymer was BBL, a ladder-type polymer processed from methane sulfonic acid.[30] Here, an electron mobility (μ_e) of 0.03 $cm^2\ V^{-1}\ s^{-1}$ and current on−off ratio ($I_{on:off}$) of 10^5 was achieved once residual acid was leached out (after annealing $\mu_e = 0.1\ cm^2\ V^{-1}\ s^{-1}$, $I_{on:off} \approx 5$). More recently, a perylene diimide-based copolymer (structure in Figure 1) FET using aluminum electrodes was reported to exhibit $\mu_e = 1.3 \times 10^{-2}$ $cm^2\ V^{-1}\ s^{-1}$ and $I_{on:off} = 10^4$ under inert atmosphere.[31] Other researchers achieved n-channel FET performance using poly(3-hexylthiophene) (P3HT) having a mobility of 6×10^{-4} $cm^2\ V^{-1}\ s^{-1}$ by employing hydrophobic dielectric coatings (to minimize charge carrier trapping at the dielectric surface) and alkali metal electrodes to reduce contact resistance. These FETs were also fabricated and characterized under inert atmosphere.[32] Polymer−oligomer blends have also been explored with reported performance as high as $\mu_e = 0.01\ cm^2\ V^{-1}\ s^{-1}$ and $I_{on:off} > 10^4$.[33] These reports and others[34] have advanced the limits of n-channel polymer performance via the synthesis of novel materials and/or implementation of unconventional and inert atmosphere device fabrication techniques.

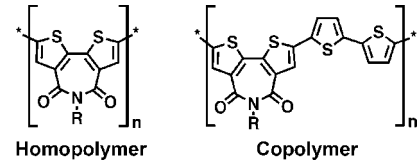

Figure 2. Structures of the **BTI**-based homopolymers and copolymers.

High-performance polymeric semiconductors must maintain a delicate balance between solubility and close, efficient $\pi-\pi$ stacking for efficient charge transport. While several p-channel polymers for OFETs meet these requirements,[14,16–18,21,22,35] achieving such performance in electron-transporting polymers has proven to be significantly more challenging. Previous efforts to enable n-channel polymer charge transport using environmentally sensitive materials and contacts or hazardous acidic solvents are not compatible with the low-cost, ambient-condition solution processing requirements essential for the realization of practical organic electronics. These studies have highlighted the need for materials having appreciable electron mobilities that are soluble in conventional organic solvents, exhibit appropriate solution rheology for printing and spin casting, and have a sufficiently high electron affinity to avoid electron trapping[32,36] by ambient species and surface states (O_2, H_2O, −OH).

The realization of n-channel polymers having the aforementioned characteristics remains a significant challenge for organic electronics since aromatic systems with appropriate electron affinity and crystallinity are typically poorly soluble, lack open positions for further substitution, and are not readily polymerizable.[23,24] To develop innovative materials that surpass such limitations, an original materials-design methodology is devised to validate favorable properties of candidate materials and evaluate structural modification options, resulting in more informed design decisions. Here we demonstrate this novel computationally aided design strategy through the development of a new class of electron-transporting polymers (Figure 2) by incorporating highly tailorable solubilizing groups into an electron-deficient core based upon the *N*-alkyl-2,2′-bithiophene-3,3′-dicarboximide unit (**BTI**).

(14) Usta, H.; Lu, G.; Facchetti, A.; Marks, T. J. *J. Am. Chem. Soc.* **2006**, *128*, 9034–9035.
(15) Sirringhaus, H.; Tessler, N.; Friend, R. H. *Science* **1998**, *280*, 1741–1744.
(16) Veres, J.; Ogier, S.; Lloyd, G.; deLeeuw, D. *Chem. Mater.* **2004**, *16*, 4543–4555.
(17) Ong, B. S.; Wu, Y.; Liu, P.; Gardner, S. *J. Am. Chem. Soc.* **2004**, *126*, 3378–3379.
(18) McCulloch, I.; Heeney, M.; Bailey, C.; Genevicius, K.; MacDonald, I.; Shkunov, M.; Sparrowe, D.; Tierney, S.; Wagner, R.; Zhang, W.; Chabinyc, M. L.; Kline, R. J.; McGehee, M. D.; Toney, M. F. *Nat. Mater.* **2006**, *5*, 328–333.
(19) Lim, E.; Kim, Y. M.; Lee, J.-I.; Byung, J.; Nam, J.; Cho, S.; Lee, J.; Do, L.-M.; Shim, H.-K. *J. Polym. Sci., Part A: Polym. Chem.* **2006**, *44*, 4709–4721.
(20) Bao, Z.; Dodabalapur, A.; Lovinger, A. J. *Appl. Phys. Lett.* **1996**, *69*, 4108–4110.
(21) Umeda, T.; Tokito, S.; Kumaki, D. *J. Appl. Phys.* **2007**, *101*, 054517.
(22) Heeney, M.; Bailey, C.; Genevicius, K.; Shkunov, M.; Sparrowe, D.; Tierney, S.; McCulloch, I. *J. Am. Chem. Soc.* **2005**, *127*, 1078–1079.
(23) Facchetti, A. *Mater. Today* **2007**, *10*, 28–37.
(24) Newman, C. R.; Frisbie, C. D.; da Silva Filho, D. A.; Bredas, J.-L.; Ewbank, P. C.; Mann, K. R. *Chem. Mater.* **2004**, *16*, 4436–4451.
(25) Bao, Z. N.; Rogers, J. A.; Katz, H. E. *J. Mater. Chem.* **1999**, *9*, 1895–1904.
(26) Gunes, S.; Neugebauer, H.; Sariciftci, N. S. *Chem. Rev.* **2007**, *107*, 1324–1338.
(27) Roncali, J. *Chem. Rev.* **1997**, *97*, 173–206.
(28) Spanggaard, H.; Krebs, F. C. *Sol. Energy Mater.* **2004**, *83*, 125–146.
(29) Huitema, H. E. A.; Gelinck, G. H.; van der Putten, J. B. P. H.; Kuijk, K. E.; Hart, C. M.; Cantatore, E.; Herwig, P. T.; van Breemen, A. J. J. M.; de Leeuw, D. M. *Nature* **2001**, *414*, 599–599.
(30) Babel, A.; Jenekhe, S. A. *J. Am. Chem. Soc.* **2003**, *125*, 13656–13657.
(31) Zhan, X.; Tan, Z.; Domercq, B.; An, Z.; Zhang, X.; Barlow, S.; Li, Y.; Zhu, D.; Kippelen, B.; Marder, S. R. *J. Am. Chem. Soc.* **2007**, *129*, 7246–7247.
(32) Chua, L. L.; Zaumseil, J.; Chang, J. F.; Ou, E. C. W.; Ho, P. K. H.; Sirringhaus, H.; Friend, R. H. *Nature* **2005**, *434*, 194–199.
(33) Letizia, J. A.; Facchetti, A.; Stern, C. L.; Ratner, M. A.; Marks, T. J. *J. Am. Chem. Soc.* **2005**, *127*, 13476–13477.
(34) Janietz, S.; Barche, J.; Wedel, A.; Sainova, D. *Macromol. Chem. Phys.* **2004**, *205*, 1916–1922.
(35) Lim, E.; Jung, B. J.; Lee, J.; Shim, H. K.; Lee, J. I.; Yang, Y. S.; Do, L. M. *Macromolecules* **2005**, *38*, 4531–4535.
(36) Yoon, M. H.; Kim, C.; Facchetti, A.; Marks, T. J. *J. Am. Chem. Soc.* **2006**, *128*, 12851–12869.

The combination of bithiophene planarity and efficient $\pi-\pi$ stacking with the electron-withdrawing capacity of the imide functionality serves as the foundation for this new class of materials. The presynthesis DFT-level computational analysis reveals that introduction of the π-electron-deficient imide moiety significantly increases monomer electron affinity, reducing the sensitivity of mobile electrons to trap states. Furthermore, geometry optimization reveals that substitution at the imide nitrogen allows introduction of functionalities with varying degrees of steric bulk while not impinging on critical intermolecular $\pi-\pi$ stacking characteristics. This motif also leaves the bithiophene 5 and 5′ positions available for polymerization. Finally, the dipole moment introduced by the imide moiety stabilizes cofacial antiparallel intra- and interchain monomer orientations, planarizing the polymer chain, enhancing $\pi-\pi$ stacking, and minimizing steric crowding by situating solubilizing groups on opposite sides of π-stacked chains. It will be seen that these unique molecular characteristics enable a balance of excellent crystallinity and efficient $\pi-\pi$ overlap with highly tunable solubility. The backbones of previously reported thiophene imide polymers based on *N*-alkyl-thiophene-3,4-dicarboximide are significantly twisted[37] with dihedral angles $> 20°$, and these materials have been shown to exhibit stable charge-transfer resonances,[38] making them suitable as low-optical bandgap donor/acceptor chromophores[39] but not useful as semiconducting materials for n-type FETs.

In the present contribution, the synthesis of the target materials is achieved using the key intermediate, bithiophene anhydride, followed by imide condensation and polymerization. Introduction of the solubilizing substituent near the conclusion of the synthetic progression allows expeditious generation of diverse homo- and copolymer libraries to evaluate the interplay of solubility, crystallinity, and charge transport. Two solution-processable polymers are obtained via this approach, which yield smooth films upon solvent casting with extraordinarily high crystallinity and a high tolerance for film deposition conditions. The annealed homopolymer exhibits excellent solubility and $\mu_e > 0.01$ cm^2 V^{-1} s^{-1} with a current on−off ratio of 10^7. The annealed copolymer exhibits a hole mobility (μ_h) of ∼0.01 cm^2 V^{-1} s^{-1} with an air-stable current on−off ratio of 10^7.

Experimental Section

Materials and Methods. All reagents were purchased from commercial sources and used without further purification unless otherwise noted. Anhydrous diethyl ether and THF were distilled from Na/benzophenone, and toluene was distilled from Na. CO_2 gas was obtained by warming dry ice and drying over P_2O_5 before use. The Stille reagent 5,5′-bis(tributylstannyl)-2,2′-bithiophene was synthesized according to a published procedure.[40] Conventional Schlenk techniques were used, and reactions were carried out under N_2 unless otherwise noted. Microwave-assisted reactions were run in sealed vessels using a CEM Discover microwave reactor in the temperature-controlled mode. UV−vis spectra were recorded on a Cary Model 1 UV−visible spectrophotometer. NMR spectra were recorded on a Varian Unity Plus 500 spectrometer (^{1}H, 500 MHz). Electrochemistry was performed on a C3 Cell Stand electrochemical station with BAS Epsilon software (Bioanalytical Systems, Inc., Lafayette, IN).

Synthesis. Synthesis of 3,3′,5,5′-Tetrabromo-2,2′-bithiophene[14,41] (1). Bromine (288 g, 1.8 mol) was added slowly over 1 h to a stirred solution of 2,2′-bithiophene (60.0 g, 0.361 mol) in 280 mL of chloroform containing 120 mL of glacial acetic acid in a 1 L round-bottom flask fitted with a reflux condenser (CAUTION: addition of the first two equivalents of bromine produces a strongly exothermic reaction). The mixture was then stirred at reflux for 12 h. Upon cooling to room temperature, a colorless precipitate was isolated by filtration and washed with methanol. The filtrate was then concentrated, and a second crop of tan precipitate was collected and washed with methanol. The combined solids were dissolved in methylene chloride (500 mL), washed four times with 200 mL of water and once with 100 mL of brine, and dried over anhydrous $MgSO_4$. The organic solution was then filtered, and the solvent was removed by evaporation to give 157 g (90% yield) of a colorless powder. ^{1}H NMR ($CDCl_3$): δ 7.06 (s, 2H) ppm.

Synthesis of 3,3′-Dibromo-2,2′-bithiophene[14,41] (2). Zn powder (31.7 g, 0.485 mol) was added in portions to a vigorously stirred refluxing mixture of bithiophene **1** (77.9 g, 0.162 mol) in 400 mL of ethanol containing 40 mL of water, 100 mL of glacial acetic acid, and 8 mL of 3 M HCl (aq). After refluxing for 2 h, the mixture was filtered hot, and upon cooling to 0 °C, yellow crystals were collected by filtration. The crystals were dissolved in diethyl ether, washed three times with 200 mL of water and once with 100 mL of brine, and dried over anhydrous $MgSO_4$. The organic solution was filtered, and the solvent was removed by evaporation to give 49.4 g (94% yield) of a light yellow powder. Anal. Calcd for $C_8H_4Br_2S_2$: C, 29.65; H, 1.24. Found: C, 29.59; H, 1.14. ^{1}H NMR ($CDCl_3$): 7.41 (d, $J = 5.3$ Hz, 2H), 7.09 (d, $J = 5.3$ Hz, 2H) ppm.

Synthesis of 2,2′-Bithiophene-3,3′-dicarboxylic Acid[42] (3). A solution of bithiophene **2** (19.44 g, 60.0 mmol) in 150 mL of diethyl ether was added dropwise over 1 h to a stirring solution of *n*-BuLi (82.5 mL, 1.6 M in hexanes) in 900 mL of ethyl ether at −78 °C. The reaction mixture was then allowed to stir for 1 h at −78 °C before dry CO_2 was bubbled into the reaction mixture for 30 min. The reaction mixture was then allowed to stir for an additional 30 min before 1 mL of methanol was added, and the reaction was filtered cold to afford a colorless solid. The solid was dried overnight in vacuo at 100 °C, dissolved in 200 mL of water, acidified with 6 M HCl (aq), and the resulting colorless precipitate isolated by filtration. This diacid was dried overnight in vacuo at 100 °C to yield 14.1 g (92% yield) of a colorless powder. Anal. Calcd for $C_{10}H_6O_4S_2$: C, 47.23; H, 2.38. Found: C, 47.19; H, 2.45. ^{1}H NMR ($CDCl_3$): 7.45 (d, $J = 4.0$ Hz, 2H), 7.10 (d, $J = 4.5$ Hz, 2H). Mp 194−198 °C. MS (EI): *m*/*z* (%) 253.79 (100) [M$^+$].

Synthesis of 2,2′-Bithiophene-3,3′-dicarboxylic Anhydride (4). Diacid **3** (12.6 g, 49.4 mmol) was stirred in 100 mL of acetic anhydride at reflux for 6 h. Upon cooling to 0 °C, the solid was collected by filtration, washed with 20 mL of cold acetic anhydride, and dried in vacuo at 120 °C overnight. The resulting light yellow crystals (11.4 g, 98% yield) were used without further purification. Anal. Calcd for $C_{10}H_4O_3S_2$: C, 50.84; H, 1.71. Found: C, 50.78; H, 1.66. ^{1}H NMR ($CDCl_3$): 7.68 (d, $J = 4.0$ Hz, 2H), 7.40 (d, $J = 5.0$ Hz, 2H). Mp 260−263 °C. MS (EI): *m*/*z* (%) 235.96 (100) [M$^+$].

Synthesis of 1-Iodo-2-octyldodecane (5). Iodine (6.06 g, 23.9 mmol) was added to a solution of 2-octyl-1-dodecanol (6.20 g, 20.8 mmol), triphenylphosphine (6.53 g, 24.9 mmol), and imidazole (1.69 g, 24.9 mmol) in 40 mL of dichloromethane at 0 °C. After stirring for 15 min, the reaction mixture was allowed to warm to room temperature over 2 h before 5 mL of sat. Na_2SO_3 (aq) was added. The organics were next concentrated by evaporation, and the mixture was taken up in 200 mL of pentane, washed three times with 100 mL of water and once with 70 mL of brine, passed through a 3 cm silica gel plug, and dried over Mg_2SO_4. The organics were concentrated by evaporation to give a light yellow oil (8.22 g, 97% yield). Anal. Calcd for $C_{20}H_{41}I$: C, 58.81; H, 10.12. Found: C, 58.70; H, 9.97. ^{1}H NMR ($CDCl_3$): 2.60 (d, $J = 5.0$ Hz, 2H), 2.00 (t, $J = 5.0$ Hz, 1H), 1.30−1.20 (b, 32H), 0.89 (t, $J = 7.5$ Hz, 6H). MS (EI): *m*/*z* (%) 408.23 (100) [M$^+$].

(37) Pomerantz, M. *Tetrahedron Lett.* **2003**, *44*, 1563–1565.
(38) Zhang, Q. T.; Tour, J. M. *J. Am. Chem. Soc.* **1997**, *119*, 9624–9631.
(39) Zhang, Q. T.; Tour, J. M. *J. Am. Chem. Soc.* **1997**, *119*, 5065–5066.
(40) Wei, Y.; Yang, Y.; Yeh, J.-M. *Chem. Mater.* **1996**, *8*, 2659–2668.
(41) Chen, W. Ph.D. Thesis, Iowa State University, 1997.
(42) Demanze, F.; Yassar, A.; Garnier, F. *Macromolecules* **1996**, *29*, 4267–4273.

Synthesis of 2-Octyldodecylamine (6). Iodoalkane **5** (5.90 g, 14.5 mmol) and potassium phthalimide (2.94 g, 15.9 mmol) were taken up in 25 mL of DMF and vigorously stirred for 72 h at 25 °C. The reaction mixture was then taken up in 200 mL of pentane, washed four times with 100 mL of water, passed through a 3 cm silica gel plug, and concentrated to give a colorless oil. The oil was next taken up in 150 mL of ethanol, 4 mL of hydrazine hydrate was added, and the mixture was refluxed overnight. The resulting precipitate was collected by filtration and dissolved in 100 mL of water, and the solution was made alkaline by addition of 6 M NaOH (aq). The resulting mixture was then taken up in 200 mL of pentane, washed four times with 100 mL of water and once with 70 mL of brine, and concentrated to give a colorless oil (3.08 g, 72% yield). Anal. Calcd for $C_{20}H_{43}N$: C, 80.73; H, 14.57. Found: C, 80.78; H, 14.52. ^{1}H NMR ($CDCl_3$): 2.60 (d, J = 5.0 Hz, 2H), 2.00 (t, J = 5.0 Hz, 1H), 1.30−1.20 (b, 32H), 0.89 (t, J = 7.5 Hz, 6H). MS (EI): m/z (%) 297.34 (100) [M^+].

Synthesis of *N*-(2-Octyldodecyl)-2,2′-bithiophene-3,3′-dicarboximide (7). A dry 8 mL microwave reaction tube was charged with a microstirbar, anhydride **4** (354 mg, 1.50 mmol), 4-(dimethylamino)pyridine (61 mg, 0.50 mmol), and 5 mL of toluene. Next, 2-octyldodecylamine (446 mg, 1.5 mmol) was added dropwise to the suspension over 15 min, and the reaction was allowed to stir for an additional 15 min until no solid remained. The reaction tube was then irradiated with microwaves (P_{MAX} = 300 W) for 2 h at a constant temperature of 220 °C. This procedure was repeated four more times, and the five reaction mixtures were combined in 250 mL of diethyl ether, washed six times with 150 mL of water and one time with 100 mL of brine, and the organics dried over Mg_2SO_4. After filtration, the solvent was removed by evaporation to afford a yellow oil (90% pure by ^{1}H NMR) that was purified by column chromatography on silica gel with a mixture of diethyl ether (10%) and hexane (90%) as the eluent. A light yellow oil (1.45 g, 37% yield) was obtained upon concentration of the main fractions. Anal. Calcd for $C_{30}H_{45}NO_2S_2$: C, 69.85. H, 8.79; Found: C, 69.79; H, 8.71. ^{1}H NMR ($CDCl_3$): 7.76 (d, J = 5.5 Hz, 2H), 7.24 (d, J = 5.5 Hz, 2H), 4.20 (t, J = 7.5 Hz, 2H), 1.71 (m, 1H), 1.37 (m, 4H), 1.26 (b, 28H), 0.89 (t, J = 7.0 Hz, 6H). MS (EI): m/z (%) 515.29 (100) [M^+]. The same procedure was followed for the synthesis of compounds **8**−**12** as described below.

Synthesis of *N*-Hexyl-2,2′-bithiophene-3,3′-dicarboximide (8). A light yellow solid (1.65 g, 69% yield) was obtained upon concentration of the main fractions. Anal. Calcd for $C_{16}H_{17}NO_2S_2$: C, 60.16; H, 5.36. Found: C, 60.05; H, 5.41. ^{1}H NMR ($CDCl_3$): 7.76 (d, J = 4.5 Hz, 2H), 7.24 (d, J = 5.5 Hz, 2H), 4.20 (t, J = 7.5 Hz, 2H), 1.71 (m, J = 8.0 Hz, 2H), 1.40 (m, 2H), 1.34 (m, 4H), 0.90 (t, J = 7.5 Hz, 3H). Mp 90−91 °C. MS (EI): m/z (%) 319.4 (100) [M^+].

Synthesis of *N*-Octyl-2,2′-bithiophene-3,3′-dicarboximide (9). A light yellow solid (1.87 g, 72% yield) was obtained upon concentration of the main fractions. Anal. Calcd for $C_{18}H_{21}NO_2S_2$: C, 62.21; H, 6.09. Found: C, 62.18; H, 3.90. ^{1}H NMR ($CDCl_3$): 7.76 (d, J = 4.5 Hz, 2H), 7.24 (d, J = 5.5 Hz, 2H), 4.20 (t, J = 7.5 Hz, 2H), 1.71 (m, J = 8.0 Hz, 2H), 1.40 (m, 2H), 1.36−1.28 (b, 10H), 0.89 (t, J = 7.5 Hz, 3H). Mp 71−72 °C. MS (EI): m/z (%) 346.9 (100) [M^+].

Synthesis of *N*-Dodecyl-2,2′-bithiophene-3,3′-dicarboximide (10). A light yellow solid (1.79 g, 59% yield) was obtained upon concentration of the main fractions. Anal. Calcd for $C_{22}H_{29}NO_2S_2$: C, 65.47; H, 7.24. Found: C, 65.31; H, 7.41. ^{1}H NMR ($CDCl_3$): 7.76 (d, J = 5.5 Hz, 2H), 7.24 (d, J = 5.5 Hz, 2H), 4.24 (m, 2H), 1.69 (m, 2H), 1.56 (m, 4H), 1.37 (m, 2H), 1.26 (b, 2H), 1.17 (m, 2H), 1.00 (d, J = 6.5 Hz, 3H), 0.87 (d, J = 6.5 Hz, 6H). Mp 60−61 °C. MS (EI): m/z (%) 403.3 (100) [M^+].

Synthesis of *N*-(4,8-Dimethylnonyl)-2,2′-bithiophene-3,3′-dicarboximide (11). A light yellow solid (1.78 g, 61% yield) was obtained upon concentration of the main fractions. Anal. Calcd for $C_{21}H_{27}NO_2S_2$: C, 64.74; H, 6.99. Found: C, 64.68; H, 7.01. ^{1}H NMR ($CDCl_3$): 7.76 (d, J = 5.5 Hz, 2H), 7.25 (d, J = 5.5 Hz, 2H), 4.20 (t, J = 7.5 Hz, 2H), 1.71 (m, 1H), 1.37 (m, 2H), 1.26 (b, 16H), 0.89 (t, J = 7.0 Hz, 9H). Mp 52−54 °C. MS (EI): m/z (%) 389.3 (100) [M^+].

Synthesis of *N*-(2-Ethylhexyl)-2,2′-bithiophene-3,3′-dicarboximide (M1, 12). A light yellow solid (1.10 g, 42% yield) was obtained upon concentration of the main fractions. Anal. Calcd for $C_{19}H_{21}NO_2S_2$: C, 62.21; H, 6.09. Found: C, 62.09; H, 6.02. ^{1}H NMR ($CDCl_3$): 7.69 (d, J = 5.5 Hz, 2H), 7.25 (d, J = 5.5 Hz, 2H), 4.20 (t, J = 7.5 Hz, 2H), 1.80 (m, J = 8.0 Hz, 1H), 1.29 (b, 8H), 0.89 (t, J = 7.5 Hz, 6H). Mp 54−56 °C. MS (EI): m/z (%) 347.1 (100) [M^+].

Synthesis of *N*-(2-Octyldodecyl)-5−5′dibromo-2,2′-bithiophene-3,3′-dicarboximide (13). Bromine (1.41 g, 8.84 mmol) was added to a solution of imide **7** (1.14 g, 2.21 mmol) in 30 mL of dichloromethane followed by addition of ferric chloride (7.2 mg, 0.044 mmol). The reaction mixture was allowed to stir in the dark for 6 h before 5 mL of sat. Na_2SO_3 (aq) was added and stirring continued for 0.5 h. The reaction mixture was then poured into 150 mL of dichloromethane, washed three times with 100 mL of water and once with 70 mL of brine, and dried over Mg_2SO_4. The organic solution was next filtered and concentrated by evaporation to give a light yellow solid (1.40, 94% yield). Anal. Calcd for $C_{30}H_{43}Br_2NO_2S_2$: 53.49; H, 6.43. Found: C, 53.36; H, 6.40. ^{1}H NMR ($CDCl_3$): 7.68 (s, 2H), 4.18 (d, J = 7.5 Hz, 2H), 1.86 (m, 1H), 1.34−1.20 (b, 32H), 0.89 (t, J = 7.5 Hz, 6H). Mp 44−46 °C. The same procedure was followed for compounds **14**−**18** as described below.

Synthesis of *N*-Hexyl-5,5′-dibromo-2,2′-bithiophene-3,3′-dicarboximide (14). A light yellow solid (84% yield) was obtained upon concentration. Anal. Calcd for $C_{16}H_{15}Br_2NO_2S_2$: C, 40.27; H, 3.17. Found: C, 40.30; H, 3.13. ^{1}H NMR ($CDCl_3$): 7.72 (s, 2H), 4.16 (t, J = 7.0 Hz, 2H), 1.69 (m, J = 7.0 Hz, 2H), 1.33−1.27 (b, 6H), 0.89 (t, J = 7.5 Hz, 3H). Mp 149−150 °C. MS (EI): m/z (%) 319.0 (100) [M^+].

Synthesis of *N*-Octyl-5,5′-dibromo-2,2′-bithiophene-3,3′-dicarboximide (15). A light yellow solid (95% yield) was obtained upon concentration. Anal. Calcd for $C_{18}H_{19}Br_2NO_2S_2$: C, 42.79; H, 3.79. Found: C, 42.66; H, 3.82. ^{1}H NMR ($CDCl_3$): 7.70 (s, 2H), 4.15 (t, J = 7.0 Hz, 2H), 1.67 (m, J = 7.0 Hz, 2H), 1.35−1.25 (b, 10H), 0.89 (t, J = 7.5 Hz, 3H). Mp 133−135 °C. MS (EI): m/z (%) 347.1 (100) [M^+].

Synthesis of *N*-Dodecyl-5,5′-dibromo-2,2′-bithiophene-3,3′-dicarboximide (16). A light yellow solid (98% yield) was obtained upon concentration. Anal. Calcd for $C_{22}H_{27}Br_2NO_2S_2$: C, 47.07; H, 4.85. Found: C, 47.05; H, 4.77. ^{1}H NMR ($CDCl_3$): 7.70 (s, 2H), 4.15 (t, J = 7.0 Hz, 2H), 1.66 (m, 2H), 1.35−1.27 (b, 18H), 0.89 (t, J = 7.0 Hz, 3H). Mp 117−119 °C. MS (EI): m/z (%) 403.3 (100) [M^+].

Synthesis of *N*-(4,8-Dimethylnonyl)-5,5′-dibromo-2,2′-bithiophene-3,3′-dicarboximide (17). A light yellow solid (92% yield) was obtained upon concentration. Anal. Calcd for $C_{21}H_{25}Br_2NO_2S_2$: C, 46.08; H, 4.60. Found: C, 45.99; H, 4.65. ^{1}H NMR ($CDCl_3$): 7.71 (s, J = 5.5 Hz, 2H), 4.15 (t, J = 7.5 Hz, 2H), 1.73 (m, 1H), 1.34 (m, 2H), 1.29 (b, 16H), 0.89 (t, J = 7.0 Hz, 9H). Mp 127−130 °C. MS (EI): m/z (%) 389.0 (100) [M^+].

Synthesis of *N*-(2-Ethylhexyl)-5,5′-dibromo-2,2′-bithiophene-3,3′-dicarboximide (18). A light yellow solid (95% yield) was obtained upon concentration. Anal. Calcd for $C_{19}H_{19}Br_2NO_2S_2$: C, 42.79; H, 3.79. Found: C, 42.57; H, 3.84. ^{1}H NMR ($CDCl_3$): 7.69 (s, 2H), 4.19 (d, J = 7.0 Hz, 2H), 1.90 (m, 1H), 1.36−1.22 (b, 8H), 0.89 (m, 6H). Mp 154−147 °C. MS (EI): m/z (%) 347.1 (100) [M^+].

Synthesis of Poly(*N*-(2-octyldodecyl)-2,2′-bithiophene-3,3′-dicarboximide) (P1). A solution of imide **23** (1.21 g, 1.80 mmol) in 70 mL of DMF was added to a solution of bis(1,5-cyclooctadiene)nickel(0) (0.594 g, 2.16 mmol), 1,5-cyclooctadiene (0.195 g, 1.80 mmol), and 2,2′-bipyridine (0.337 g, 2.16 mmol) which had been stirring for 20 min in 10 mL of DMF. The reaction mixture

was then heated at 60 °C for 48 h before bromobenzene (2.83 g, 18.0 mmol) was added, and the reaction mixture was allowed to stir for an additional 12 h. The mixture was then allowed to cool to room temperature, poured into 200 mL of methanol containing 20 mL of 12 M HCl (aq), and stirred for 6 h; the precipitate was collected by filtration and dried overnight in vacuo at 120 °C to give 0.970 g of solid. The crude product was next dissolved in 40 mL of toluene, filtered through a 0.45 μm filter, precipitated with 400 mL of methanol, collected by filtration, and dried as before to give 0.912 g of dark red powder. This precipitation procedure was repeated four more times to give 0.821 g of dark red powder, which was placed in a microscale Soxhlet extractor and extracted for 48 h with methanol, 24 h with pentane, and recovered by extraction with dichloromethane. The dichloromethane solution was filtered through a 0.22 μm filter, and the polymer precipitated with 300 mL of methanol to give **5** as a red powder (0.634 g) after drying in vacuo at 120 °C. Anal. Calcd for $C_{30}H_{43}NO_2S_2$: C, 70.13; H, 8.44; N, 2.73. Found: C, 69.94; H, 8.69; N, 2.89. ^{1}H NMR ($CDCl_3$): 7.71 (b, 2H), 4.25 (b, 2H), 1.88 (b, 1H), 1.4−1.2 (b, 32H), 0.89 (t, J = 7.5 Hz, 6H). GPC (150 °C, TCB, vs PS): $M_w = 7.9 \times 10^3$. PDI = 2.2. Attempts to prepare homopolymers were carried out using the same Yamamoto polymerization conditions with monomers **15**−**18**, yielding completely insoluble products. Polymerizations of **15**−**18** were also performed under milder conditions (30 °C, 1−2 h), also resulting in intractable products.

Synthesis of Poly(*N*-(2-octyldodecyl)-2,2′:5′,2″:5″,2‴-quaterthiophene-3,3′-dicarboximide) (P2). Imide **13** (0.674 g, 1.00 mmol), 2,5′-bis(tributylstannyl)-2,2′-bithiophene (0.744 g, 1.00 mmol), and $Pd(PPh_3)_4$ (0.045 g, 0.050 mmol) in anhydrous DMF (20 mL) were heated at 90 °C under nitrogen for 24 h. The reaction mixture was then allowed to cool to room temperature and poured into 300 mL of methanol, and the precipitate was collected by filtration to give 0.621 g of black solid. The crude material was placed in a microscale Soxhlet extractor and extracted for 48 h with methanol and 24 h with pentane, and it was recovered by extraction with chlorobenzene. The chlorobenzene solution was passed through a 0.22 μm filter, and the polymer precipitated with 200 mL of methanol to give **P2** as a purple solid (0.107 g, 16% yield) after drying in vacuo at 120 °C. Anal. Calcd for $(C_{38}H_{47}NO_2S_4)_n$: C, 67.31; H, 6.99; N, 2.07. Found: C, 67.04; H, 7.11; N, 1.99. ^{1}H NMR ($C_2D_4Cl_4$): 8.09 (b, 2H), 7.20 (b, 4H), 4.32 (b, 2H), 2.05 (b, 1H), 1.35 (b, 32H), 0.96 (b, 6H). GPC (150 °C, TCB, vs PS): $M_w = 2.5 \times 10^3$. PDI = 1.38. Attempts to copolymerize **15**−**18** and 2,5′-bis(tributylstannyl)-2,2′-bithiophene were carried out using the same procedure and yielded insoluble products. Copolymerizations of **15**−**18** with 2,5′-bis(tributylstannyl)-2,2′-bithiophene using milder conditions were also attempted (30 °C, 1−12 h), all resulting in intractable products.

Synthesis of *N*-Hexyl-2,2′:5′,2″:5″,2‴-quaterthiophene-4′,3″-dicarboximide (19). A dry 8 mL microwave reaction tube was charged with a microstirbar, imide **14** (0.416 g, 0.871 mmol), 2-(tributylstannyl)thiophene (0.650 g. 1.74 mmol), $Pd(PPh_3)_4$ (0.041 g, 0.045 mmol), and DMF (6 mL) before being irradiated with microwaves (P_{MAX} = 300 W) for 5 min at a constant temperature of 120 °C. Upon cooling, the orange precipitate was collected by filtration, washed with methanol (10 mL), and dried in vacuo at 120 °C. The solid was purified by column chromatography on silica gel with a mixture of diethyl ether (30%) and hexane (70%) as the eluent. Orange (0.153 g) needle-like crystals were obtained upon concentration of the main fractions. The crystals were further purified by sublimation under vacuum to give orange needle-like crystals (0.111 g, 26% yield) suitable for single-crystal diffraction. Anal. Calcd for $(C_{24}H_{21}NO_2S_4)_n$: C, 59.60; H, 4.38. Found: C, 59.53; H, 4.34. ^{1}H NMR ($CDCl_3$): 7.81 (s, 2H), 7.34 (d, 4.5 Hz, 2H), 7.26 (d, 4.0 Hz, 2H), 4.21 (t, J = 8.0 Hz, 2H), 1.72 (m, 2H), 1.43 (m, 2H), 1.36 (b, 6H), 0.91 (t, J = 7.0 Hz, 3H). Mp 190−193 °C. MS (EI): m/z (%) 483.1 (100) [M^+].

Synthesis of *N*-(2-Ethylhexyl)-2,2′:5′,2″:5″,2‴-quaterthiophene-4′,3″-dicarboximide (M2). A dry 8 mL microwave reaction tube was charged with a microstirbar, imide **18** (0.445 g, 0.871 mmol), 2-(tributylstannyl)thiophene (0.650 g. 1.74 mmol), $Pd(PPh_3)_4$ (0.041 g, 0.045 mmol), and DMF (6 mL) before being irradiated with microwaves (P_{MAX} = 300 W) for 5 min at a constant temperature of 120 °C. Upon cooling, an orange precipitate was collected by filtration, washed with methanol (10 mL), and dried in vacuo at 120 °C. The solid was purified by column chromatography on silica gel with a mixture of diethyl ether (30%) and hexane (70%) as the eluent to yield 0.153 g of orange needle-like crystals upon concentration of the main fractions. The crystals were further purified by sublimation under vacuum to give orange needle-like crystals (0.136 g, 22% yield). Anal. Calcd for $C_{26}H_{25}NO_2S_4$: C, 61.02; H, 4.92. Found: C, 60.89; H, 4.78. ^{1}H NMR ($CDCl_3$): 7.82 (s, 2H), 7.35 (d, 4.5 Hz, 2H), 7.26 (b, 2H), 4.27 (m, 2H), 1.87 (m, 1H), 1.38−1.26 (m, 8H), 0.92 (m, 6H). Mp 181−184 °C. MS (EI): m/z (%) 511.2 (100) [M^+].

Polymer Molecular Weight Determination. GPC measurements were performed on a Polymer Laboratories PL-GPC 220 instrument using 1,2,4-trichlorobenzene as the solvent (stabilized with 125 ppm BHT) at 150 °C. A set of three PLgel 10 μm mixed columns was used. Samples were prepared at 160 °C. Molecular weights were determined by GPC using narrow polystyrene standards and not corrected.

Electrochemistry. Cyclic voltammetry measurements were performed with a 0.1 M tetrabutylammonium hexafluorophosphate electrolyte in dry acetonitrile for polymer films and in THF for molecules in solution. Platinum electrodes were used as both working and counter electrodes, and an Ag wire was used as the pseudoreference electrode. A ferrocene/ferrocenium redox couple was used as an internal standard, and potentials obtained in reference to the silver electrode were converted to the saturated calomel electrode (SCE) scale. Thin films of the polymers were coated onto the Pt working electrode by drop casting from 0.1 wt % THF or 1,2-dichlorobenzene solutions and dried under vacuum at 80 °C for 2 h.

Thermal Characterization. Polymers were dried under vacuum for 3 days at 120 °C before thermal analysis. Thermogravimetric analysis (TGA) was performed on a TA instruments Q50 at a ramp rate of 5 °C/min under nitrogen at atmospheric pressure in an aluminum oxide crucible. Differential scanning calorimetry (DSC) was performed using a Mettler Toledo DSC823e instrument at a ramp rate of 10 °C/min using aluminum pans under nitrogen.

Device Fabrication and Measurement. Prime-grade p-doped silicon wafers (100) having 300 nm thermally grown oxide (Process Specialties Inc.) were used as device substrates. These were sonicated in methanol, acetone, propanol, and oxygen plasma cleaned before film deposition. Trimethylsilyl functionalization of the SiO_2 surface was carried out by exposing the cleaned silicon wafers to hexamethyldisilazane (HMDS) vapor under nitrogen at room temperature for 4 days. Films of **P1** were spin coated from 0.5% (w/v) THF, $CHCl_3$, or 1,2,4-trichlorobenzene solutions, and films of **P2** were spin coated from 0.5% (w/v) 1,2-dichlorobenzene solutions at 50 °C. All films were dried at 120 °C in vacuo for 12 h and, if annealed, heated under nitrogen at various temperatures from 180 to 300 °C for 30 min or 2 h, as specified in the text. Spin-coated polymer films were 20−37 nm thick as determined by profilometry. For FET device fabrication, top-contact gold electrodes (500 Å) were deposited by thermal evaporation through a shadow mask to define channels with dimensions 100 μm (L) by 2.00 mm (W). The capacitance of the 300 nm SiO_2 insulator is 1×10^{-8} F/cm^2, and mobilities were calculated in the saturation regime. TFT device measurements were carried out at 21−23 °C in a customized high-vacuum probe station (1×10^{-6} Torr) or in air. Coaxial and/or triaxial shielding was incorporated into Signaton probes to minimize noise levels. TFT characterization was performed with a Keithley 6430 subfemtoampmeter (drain) and a

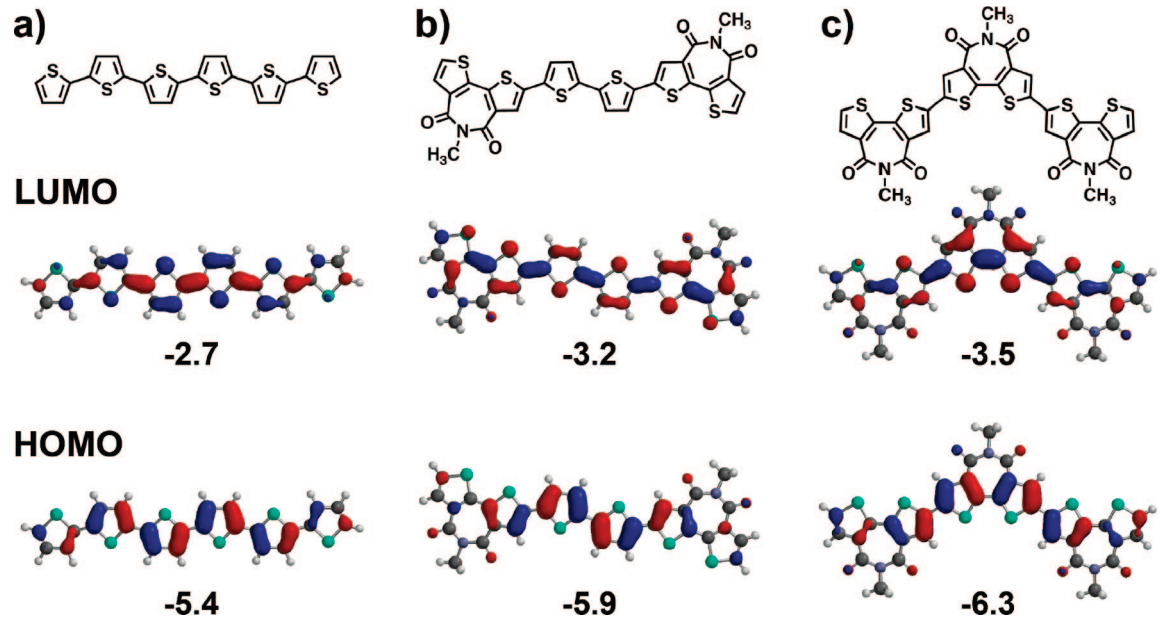

Figure 3. DFT-optimized geometries, frontier orbitals, and orbital energies (eV vs vacuum) of sexithiophene (a) and the indicated oligomers having two (b) or three (c) imide units.

Table 1. Summary of Optical Absorption Data for Monomers **M1**, **M2**, **P1**, and **P2**

	experimental							calculated[d]	
	λ_{max}^{soln} (nm)	$\lambda_{shoulder}^{soln}$ (nm)	λ_{max}^{film} (nm)	$\lambda_{shoulder}^{film}$ (nm)	E_{gap}[a] (eV)	HOMO[b] (eV)	LUMO[c] (eV)	HOMO (eV)	LUMO (eV)
M1	348	367	351	371, 501, 602	3.2	−6.43[d]	−3.23		
M2	432	454	455	428, 489	2.5	−5.94	−3.11		
P1	535	503, 578	524	498, 564	2.0	−6.28	−3.47	−6.25	−3.52
P2	517	366, 553, 607	615	390, 517, 569	1.9	−5.88	−3.04	−5.90	−3.18

[a] Optical band gap calculated from the red edge of the S_0-S_1 absorption band at 1/10 of the maximum intensity. [b] HOMO energy estimated by subtracting the optical gap from the LUMO energy. [c] Estimated from the onset of the first reduction using the correction factor −4.4 V to convert SCE reference to vacuum.[45] [d] Calculated using DFT for oligomers in Figure 3 and corrected with the HOMO/LUMO energies of sexithiophene[44] estimated from solution electrochemistry.

Keithley 2400 (gate) source meter, operated by a locally written Labview program and GPIB communication.

Thin-Film Characterization. Thin films were analyzed by wide-angle X-ray film diffractometry (WAXRD) on a Rikagu ATX-G instrument using standard $\theta-2\theta$ techniques with Cu Kα_1 radiation. Atomic force microscopy was performed on a Jeol 5200 SPM instrument. Scanning electron microscopy was performed on a Hitachi 4800 SEM with samples having a 2 nm Au/Pd sputtered film.

Computational Methodology. Equilibrium geometry optimizations were performed in QChem 2.1[43] using density functional theory DFT with a B3LYP functional and the 3-12G* basis set. Single-point calculations using these geometries were then performed at the DFT/B3LYP/6-31+G* level of theory to obtain molecular orbital energy levels (QChem) and molecular orbital electron density plots (Spartan '06). Energy levels were calibrated to the experimental HOMO/LUMO energies[44] of sexithiophene. Dipole moments for **M1** and **M2** were calculated using UHF/6-31+G* with DFT-optimized geometries.

Results

The **BTI** materials are first evaluated computationally, and their optimized geometries, MO energy levels, and orbital electron density plots are reported. Next, the six-step monomer synthetic route is described followed by the synthesis of model compounds and polymers. The materials obtained are next characterized by GPC, electronic absorption spectroscopy, and electrochemistry. WAXRD, SEM, and AFM are then employed to characterize spin-cast polymer film microstructure, followed by FET device fabrication and optimization. Finally, the crystal structure of a molecular model compound is described in detail.

Table 2. Anodic (E_a), Cathodic (E_c), and Half-Wave ($E^{1/2}$) Potentials (V vs SCE) from Cyclic Voltammetry of **M1**, **M2**, **P1**, and **P2**

	oxidation			reduction					
	cathodic[a]			cathodic		anodic		half-wave	
compound	E_{c1}	E_{c2}	E_{c3}	E_{c1}	E_{c2}	E_{a1}	E_{a2}	$E_1^{1/2}$	$E_2^{1/2}$
M1[b]				−1.47		−1.83		−1.65	
M2[b]	1.54	1.77		−1.27		−1.48		−1.38	
P1[c]	1.71	1.88	1.97	−1.01	−1.26	−1.21	−1.38	−1.11	−1.32
P2[c]	1.48	1.67	2.00	−1.27	−1.44	−1.42	−1.64	−1.34	−1.54

[a] Oxidation events are irreversible. [b] Electrochemistry performed in THF solution. [c] Electrochemistry performed on films on Pt electrode.

Quantum Chemical Modeling. The geometries of a **BTI** trimer, **BTI**-bithiophene-**BTI** co-oligomer, and sexithiophene were optimized at the DFT/B3LYP/3-21G* level, revealing a highly planar **BTI** $\pi-$core with negligible intermonomer torsion (Figure 3). The imides are found to be oriented antiparallel in both **BTI**-containing oligomers, and there is negligible interaction of the imide nitrogen substituent with neighboring subunits. Using the optimized geometries, the molecular orbital energies

(43) Pople, J. A.; et al. *J. Comput. Chem.* **2000**, *21*, 1532–1548.
(44) Facchetti, A.; Hutchison, G. R.; Yoon, M. H.; Letizia, J.; Ratner, M. A.; Marks, T. J. *Abstr. Pap. Am. Chem. Soc.* **2004**, *227*, U448−U448.

Scheme 1. General Synthetic Route to 2,2′-Bithiophene-3,3′-dicarboximide Monomers

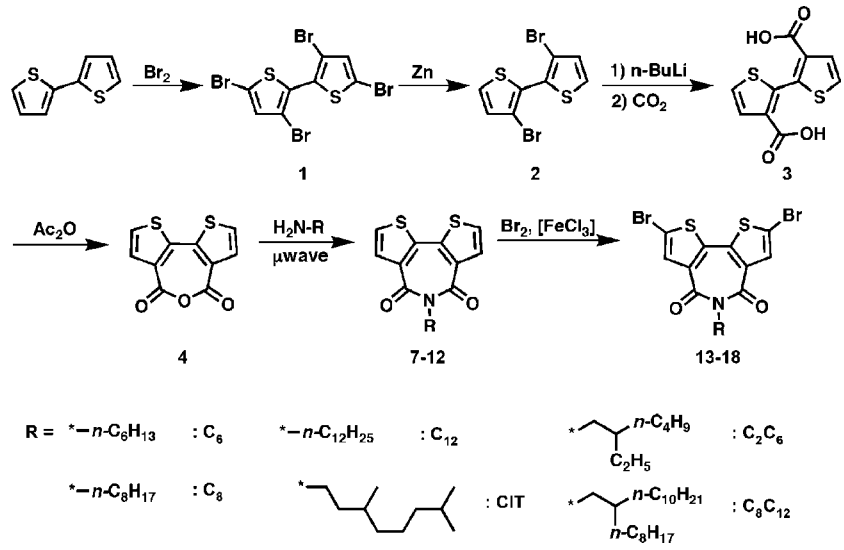

Scheme 2. Synthesis of Molecular Model Compounds *N*-Hexyl-2,2′:5′,2″:5″,2‴-quaterthiophene-4′,3″-dicarboximide (**19**) and *N*-(2-Ethylhexyl)-2,2′:5′,2″:5″,2‴-quaterthiophene-4′,3″-dicarboximide (**M2**)

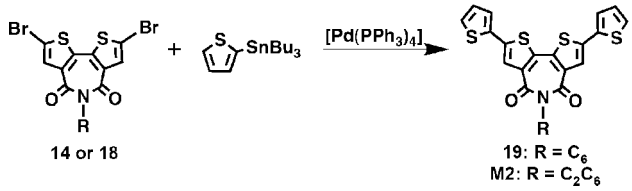

were calculated using the 6-31+G* basis. Energies reported in Figure 3 and summarized in Table 2 were obtained by correcting the DFT-derived eigenvalues to the HOMO and LUMO energies of sexithiophene,[44] estimated[45] from electrochemical data. Molecular orbital plots reveal highly delocalized HOMOs and LUMOs having aromatic and quinodal configurations, respectively. The **BTI** trimer LUMO energy is lowest at −3.52 eV, while that of the co-oligomer lies at −3.18 eV, both lower than that of sexithiophene at −2.69 eV. Sexithiophene is found to have the highest lying HOMO at −5.38 eV, followed by the co-oligomer at −5.90 eV, and the **BTI** trimer at −6.25 eV. Finally, the dipole moments of **M1** and **M2** are calculated to be 2.27 and 3.78 Debye, respectively, oriented toward the imide nitrogen atom.

Synthesis. The dibromo-functionalized **BTI** building blocks **13**−**18** were all prepared from commercially available 2,2′-bithiophene according to Scheme 1. Model molecular compounds **19** and **M2** were obtained according to Scheme 2 by Stille coupling of 2-(tributylstannyl)thiophene with reagents **14** and **18**, respectively, and purified by column chromatography and sublimation. Crystals of **19** suitable for single-crystal diffraction were obtained by slow sublimation at 50 mTorr onto a coldfinger. Yamamoto and Stille coupling polymerizations were employed to synthesize the homopolymers and bithiophene copolymers, respectively, as shown in Scheme 3. The key intermediate, bithiophene anhydride (**4**), was synthesized in four steps from 2,2′-bithiophene.

First, 2,2′-bithiophene was tetrabrominated by refluxing with Br_2 in a mixture of chloroform and acetic acid to give 3,5,3′,5′-tetrabromo-2,2′-bithiophene **1**, which was then selectively debrominated with Zn to yield 3,3′-dibromo-2,2′-bithiophene **2**. To obtain the corresponding dicarboxylic acid, **2** was slowly added to a dilute solution of *n*-BuLi followed by quenching of the dilithium salt with dry carbon dioxide to afford the dilithium salt of 3,3′-dicarboxylate-2,2′-bithiophene. Diacid **3** was obtained upon acidification of the solid and used without further purification. Condensation/cyclization of **3** was carried out in refluxing acetic anhydride to yield the novel key intermediate 2,2′-bithiophene-3,3′-dicarboxylic anhydride **4** in 77% overall yield from 2,2′-bithiophene. Six imides were then synthesized by condensation of **4** with primary amines. Of the amines used, only 2-octyldodecylamine was synthesized, while the remaining are commercially available. The reagent 2-octyldodecylamine

Scheme 3. Synthesis of **BTI** Homopolymers and Copolymers

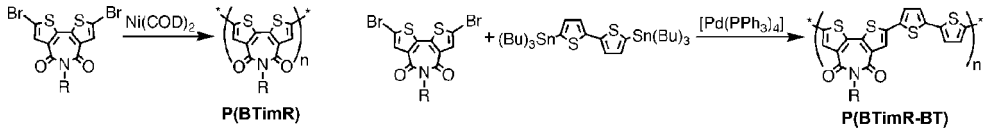

	P(BTimR) Homopolymer Yield		P(BTimR-BT) Copolymer Yield	
R	Solubility	Purified	Solubility	Purified
C_8C_{12}	99%	69%	18%	13%
C_8	<1%	-	<1 %	-
C_{12}	~1%	-	<1 %	-
CIT	~2%	-	~1%	-
C_2C_6	~1%	-	<1 %	-

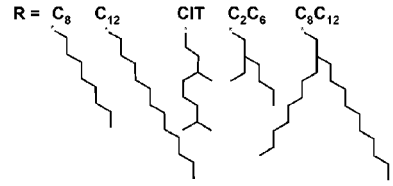

amine was obtained in 70% overall yield via iodination of the commercially available alcohol to **5**, followed by a Gabriel synthesis to yield 2-octyldodecylamine (**6**).

Imide condensations of the novel seven-membered anhydride **4** with primary alkyl amines were initially performed in molten imidazole. However, the required temperature of 200 °C and reaction times over 12 h resulted in significant decomposition of the imide to the corresponding diamide, resulting in <5% yields when sterically hindered amines were used.[46] Other imide condensation conditions were explored without success, including removal of water by azeotroping and condensation in refluxing propionic acid.[47] The most efficient method found for synthesizing the unique seven-membered *N*-akyl-2,2′-bithiophene-3,3′-dicarboximides **7**−**12** was by microwave irradiation for 2 h in toluene with a catalytic amount of 4-(dimethylamino)pyridine at a temperature of 220 °C. The crude products were purified by column chromatography to afford the pure imides in yields ranging from 72% for *n*-alkyl amines to 37% for branched-alkyl primary amines. Finally, the dibromo-functionalized monomers **13**−**18** were synthesized in quantitative yield by addition of Br_2 to a solution of the imides in dichloromethane containing a catalytic amount of ferric chloride.

Polymers were synthesized according to Scheme 3 from the dibromo-functionalized imides **13**, **15**−**17**, and 5,5′-bis(tributylstannyl)-2,2′-bithiophene. Homopolymers were obtained by Yamamoto polycondensation of **13** or **15**−**18** for 48 h in DMF at 60 °C in a procedure similar to previous reports using electron-deficient bromo-functionalized heterocycles.[48] Polymers were isolated by filtration after quenching the reaction mixture with acidic methanol, and the soluble homopolymer **P1** was purified by multiple precipitations from chloroform with methanol. Products obtained from reactions using the less bulky imides **15**−**18** were found to be insoluble. To reduce molecular weights, polymerizations were also carried out under milder reaction conditions (30 °C, 1−2 h). Attempts to isolate tractable materials by Soxhlet extraction were unfruitful, with only 1−2% of the crude products extracted using 1,2-dichlorobenzene, after washing with methanol and pentane. Copolymers of **13** and **15**−**18** with bithiophene were synthesized by Stille coupling using either standard polymerization conditions (90 °C, 24 h) or milder reaction conditions (30 °C, 1−12 h). Crude reaction precipitates were isolated by filtration, and solubility was evaluated by Soxhlet extraction with methanol (48 h) and pentane (24 h), followed by redissolution of the polymer in chlorobenzene. Polymer **P2** was isolated by this method, followed by precipitation from chlorobenzene with methanol. Copolymers synthesized with **15**−**18**, even under mild conditions, were found to be intractable. The structures of the π-conjugated monomers and polymers synthesized and characterized in this study, **M1**, **M2**, **P1**, and **P2**, are shown in Figure 4.

Polymer Molecular Weight. Gel permeation chromatography (GPC) was used to determine polymer molecular weight versus polystyrene. **P1** was found to have M_w = 7900 D and PDI = 2.2 and **P2** to have M_w = 2500 D and PDI = 1.4. These data suggest a mean chain length of ∼15 monomer units (∼30 thiophene rings) for polymer **P1** and ∼4 monomer units (∼16 thiophene rings) for polymer **P2**.

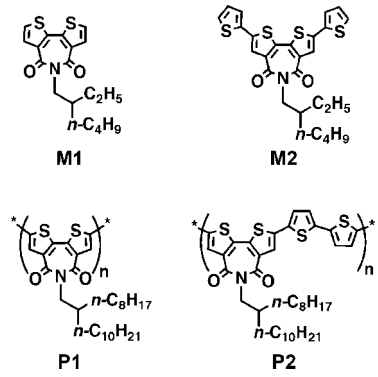

Figure 4. Structures of π-conjugated monomers and polymers **M1**, **M2**, **P1**, and **P2**.

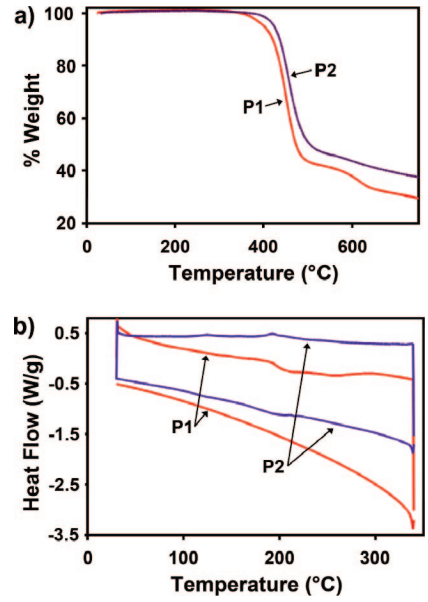

Figure 5. Thermogravimetric analysis (TGA, a) and differential scanning calorimetry (DSC, b) plots for homopolymer **P1** (red) and copolymer **P2** (purple). The first DSC cycle is shown for **P1**, while the second cycle is shown for **P2**.

Polymer Thermal Properties. Thermogravimetric analysis (TGA) was used to evaluate the thermal stability of purified polymers **P1** and **P2** (Figure 5a). A mass loss of 5% is defined as the threshold for thermal decomposition. Both materials demonstrate good thermal stability with the onset of decomposition at 401 °C for **P1** and 424 °C for **P2**.

Differential scanning calorimetry (DSC) was used to characterize the thermal transitions in the polymers (Figure 5b). Homopolymer **P1** exhibits a glass transition-like feature at 201 °C and a broad endothermic transition at 295 °C on the forward sweep of the first DSC cycle. Since no thermal transitions are observed on the reverse sweep or in any of the subsequent cycles, these features indicate irreversible **P1** relaxation phenomena. Copolymer **P2** undergoes two reversible endothermic transitions at 127 and 196 °C. Both of these transitions are reversible with exotherms at 197 and 120 °C in the reverse sweeps over four cycles.

Polymer Optical Properties. Solution and thin-film UV−vis absorption spectra of the present monomers and the corresponding polymers are shown in Figure 6, and the optical spectroscopic data are summarized in Table 1. In chlorobenzene solution, molecules **M1** and **M2** exhibit absorption maxima at

(45) Agrawal, A. K.; Jenekhe, S. A. *Chem. Mater.* **1996**, *8*, 579–589.
(46) Wescott, L. D.; Mattern, D. L. *J. Org. Chem.* **2003**, *68*, 10058–10066.
(47) Abdalla, M. A.; Bayer, J.; Raedler, J. O.; Muellen, K. *Angew. Chem., Int. Ed.* **2004**, *43*, 3967–3970.
(48) Yamamoto, T.; Saito, N. *Chem. Lett.* **1996**, *25*, 127–128.

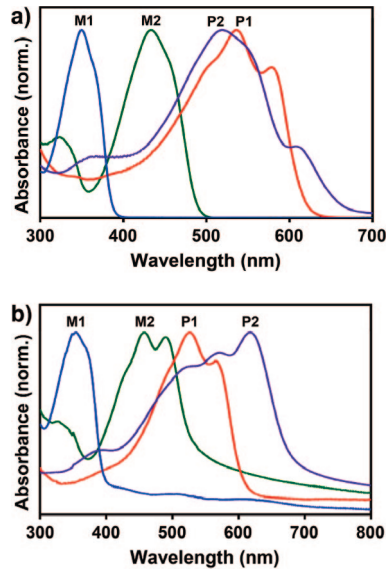

Figure 6. Optical absorption spectra of monomers **M1** (blue), **M2** (green), homopolymer **P1** (red), and copolymer **P2** (purple) in chlorobenzene solution (a) and as thin films cast from chlorobenzene on quartz (b). Data are collected in Table 1.

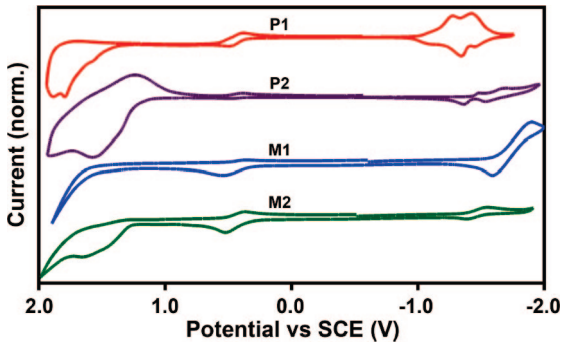

Figure 7. Cyclic voltammograms of **M1** (blue), **M2** (green), homopolymer **P1** (red), and copolymer **P2** (purple). Data are collected in Table 2.

348 and 432 nm, respectively, with a shoulder on the red side of the band ~20 nm from the peak maximum. **M1** thin films exhibit a maximum absorption at 351 nm and a shoulder at 371 nm (similar to that in solution), while **M2** films have a maximum at 455 nm and shoulders at 428 and 489 nm. Homopolymer **P1** exhibits an absorption maximum at 535 nm in chlorobenzene with shoulders at 503 and 578 nm. The thin-film spectrum of this polymer is similar, with a maximum at 524 nm and shoulders at 498 and 564 nm. The solution absorption spectrum of **P2** has a maximum at 517 nm

Shoulders appear at 336, 553, and 607 nm. Similar to the thiophene-substituted molecule, the **P2** red absorption bands are enhanced in the thin-film spectrum with a maximum at 615 nm and shoulders at 390, 517, and 569 nm

Electrochemical Properties. The redox behavior of **M1**, **M2**, **P1**, and **P2** was investigated using cyclic voltammetry (Figure 7, Table 2). All potentials are reported vs SCE with the ferrocene/ferrocenium couple used as an internal standard. **M1** exhibits the onset of reduction at −1.17 V with a reversible reduction wave at −1.65 V. A significant oxidation wave is not observed for this material. Thiophene-substituted molecule **M2** shows the onset of reduction at −1.29 V with a reversible reduction wave at −1.65 V. The onset of oxidation is found to be at 1.39 V with two partially reversible events at 1.54 and 1.77 V. Homopolymer **P1** films on Pt exhibit multiple reversible reduction waves with onset at −0.93 V and half-wave potentials of −1.11 and −1.32 V. Oxidation of the homopolymer occurs with an onset of 1.42 V with two irreversible events at 1.88 and 1.97 V. Copolymer **P2** thin films exhibit two reversible reduction events with onset at −1.36 V and half-wave potentials at −1.34 and −1.54 V. Oxidation of the homopolymer thin films occurs with an onset at 1.19 V and three irreversible oxidations with half-wave potentials at 1.39, 1.48, and 1.92 V.

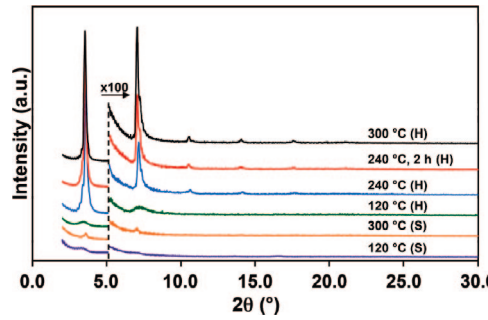

Figure 8. X-ray diffraction $\theta-2\theta$ plots of homopolymer **P1** films spin-cast from $CHCl_3$ onto hydrophilic SiO_2 (S) and hydrophobic HMDS treated (H) substrates, then annealed at the indicated temperatures for 30 min unless otherwise noted.

Thin-Film X-ray Diffraction Analysis. Thin-film wide-angle X-ray diffraction (XRD) $\theta-2\theta$ scans of homopolymer **P1** and copolymer **P2** were performed to investigate the degree of film crystallinity and the polymer chain orientation with respect to the substrate surface. Films were cast on the same substrates (p^{+2}-Si/300 nm SiO_2, untreated or HMDS treated) used to fabricate TFTs (vide infra), then dried, and annealed between 120 and 300 °C as specified. **P1** films exhibit several strong Bragg reflections on the HMDS-treated substrates (Figures 8, S1, and S2), while less intense reflections are observed from films on the untreated substrates. XRD intensities increase, and higher-order peaks are observed in all films when the annealing time and/or temperature is increased. In all films of the homopolymer, a single family of Bragg peaks is observed corresponding to a d spacing of 25.1 ± 0.6 Å with up to fifth-order reflections observed from films on hydrophobic substrates. This d spacing corresponds to **P1** chains angled at ~69.0° relative to the substrate plane if the chains are not interdigitated from one layer to the next.[49] Laue oscillations are observed at low angles for films cast from TCB.

Films of copolymer **P2** also exhibit strong Bragg reflections (Figure 9). Copolymer films on untreated SiO_2 substrates exhibit broad first- and second-order reflections with the intensities increasing with annealing temperature. Films on HMDS-treated substrates exhibit more intense diffraction features, having narrower peaks and reflections up to third order for films annealed at higher temperatures. The Bragg reflections observed in all films indicate highly crystalline films with a d spacing of 21.7 ± 0.1 Å along the substrate normal. This d spacing corresponds to the polymer chains angled at ~54° relative to the substrate plane if the chains are not interdigitated from one layer to the next. The estimated tilt angle relative to the plane will be less if the chains are interdigitated between layers.[49]

Film Surface Microstructure. Scanning electron microscopy (SEM) and tapping-mode atomic force microscopy (AFM) were

(49) Kline, R. J.; DeLongchamp, D. M.; Fischer, D. A.; Lin, E. K.; Richter, L. J.; Chabinyc, M. L.; Toney, M. F.; Heeney, M.; McCulloch, I. *Macromolecules* **2007**, *40*, 7960–7965.

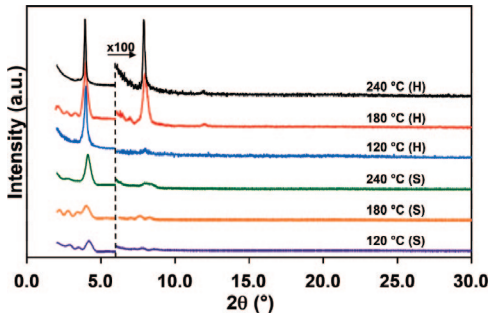

Figure 9. X-ray diffraction $\theta-2\theta$ plots of copolymer **P2** spin-cast film from 1,2-dichlorobenzene onto hydrophilic SiO_2 (S) and hydrophobic HMDS-treated (H) substrates then annealed at various temperatures for 30 min.

employed to evaluate the polymer film continuity, surface morphology, and roughness. Films of **P1** cast from all solvents on HMDS-treated substrates are continuous with the roughness and surface morphology being highly dependent on the casting solvent (Figure 10 and Supporting Information Figures S3 and S4). Casting from TCB solutions yields films with 2.6 nm rms roughness (after drying at 120 °C). Additional annealing results in a slightly decreased 1.8 nm rms roughness and the appearance of terracing in the polymer films with a step height of 2.5 nm as determined from AFM height histograms (Figure 11). Films cast from chloroform solutions contain large circular holes in otherwise featureless films after drying (17 nm rms roughness). The holes disappear with annealing, and SEM and AFM images reveal smooth, continuous, polycrystalline films with rms roughness increasing with annealing temperature from 1.8 nm at 240 °C to 4.4 nm at 300 °C. Films cast from THF exhibit the greatest rms roughnesses (29 nm) with irregularly shaped solvent pockets in samples dried at 120 °C that decrease in size with annealing to yield a highly textured film when annealed at 240 °C for 2 h or 300 °C for 30 min. All homopolymer films cast on untreated SiO_2 substrates are featureless without evidence of solvent bubbles or crystallization (Supporting Information Figures S5, S6, and S7).

Films of **P2** were spin cast from DCB solutions at 0 °C and evidence continuous surface coverage upon drying. Those cast on untreated SiO_2 surfaces have an initial rms roughness of 1.2 nm which decreases with annealing to 1.0 nm (Supporting Information, Figure S8). Films cast onto HMDS-treated substrates exhibit a greater initial rms roughness of 4.0 nm, which increases with annealing to 5.8 (180 °C) and 8.4 nm (240 °C) (Figure 12a−f). This increase in roughness corresponds to melting of the polymer followed by dewetting from the hydrophobic surface as evidenced by large gaps appearing in the film when annealed at 180 °C. Only islands of polymer are present once the sample is annealed at 240 °C (Figure 12c,f). Cross-polarized hot-stage optical microscopy of **P2** films cast on untreated glass reveal a crystalline phase at temperatures below a liquid-crystalline transition at 127 °C (Figure 12g), the liquid crystalline phase (Figure 12h), and finally the melting transition of the **P2** film at 196 °C (Figure 12i).

Transistor Fabrication and Optimization. Thin-film transistors were fabricated with spin-cast and drop-cast films of polymers **P1** and **P2** as the semiconducting component. FETs fabricated with either material were initially evaluated under vacuum. Homopolymer **P1** exhibits exclusively n-type transport in this geometry, while copolymer **P2** exhibits only p-type behavior under vacuum (Figure 13). When the devices are measured under air, the homopolymer does not exhibit FET activity and the copolymer accumulation regime p-channel FET behavior is unchanged. Semiconductors cast onto HMDS-treated substrates exhibit superior performance, while those on untreated SiO_2 substrates exhibit diminished performance in the case of **P2** or negligible FET activity in the case of **P1**.

Polymer film microstructure was adjusted to optimize device performance by casting from various solvents ($CHCl_3$, THF, TCB, or DCB), employing different substrate functionalizations and thermal annealing protocols to enhance crystallinity. Annealing temperatures were optimized from the thermal transitions observed in the DSC. Homopolymer **P1** was spin cast from $CHCl_3$, THF, and TCB onto both HMDS-treated and untreated substrates. Films cast on the hydrophilic untreated substrates do not exhibit FET activity, while those cast onto hydrophobic substrates exhibit prototypical n-channel FET behavior (Table 3). Film electron mobilities (μ_e) after the initial drying at 120 °C vary from $\sim 5 \times 10^{-4}$ cm^2 V^{-1} s^{-1} for films from TCB and THF to 2×10^{-3} cm^2 V^{-1} s^{-1} for films from $CHCl_3$. Upon annealing, μ_e and $I_{on:off}$ increase, with the highest μ_e of 0.011 $\pm$ 0.003 cm^2 V^{-1} s^{-1} observed in films cast from $CHCl_3$ and annealed at 240 °C for 2 h ($I_{on:off} = 2 \times 10^7$, $V_T = +75$ V). Device performance decreases in all samples when films are annealed at 300 °C. Drop-cast films exhibit performance similar to that of spin-cast films with mobilities of 0.003 cm^2 V^{-1} s^{-1} when cast from $CHCl_3$ and annealed at 120 °C.

Since **P2** only has adequate solubility in DCB, annealing and substrate treatment were the two variables that were varied during device optimization. All films of **P2** cast on hydrophobic HMDS-treated substrates exhibit hole mobilities 2 orders of magnitude greater than those on untreated hydrophilic SiO_2 (Table 4). When samples are annealed at 180 °C, the mobility increases on both substrates up to 0.008 cm^2 V^{-1} s^{-1} ($I_{on:off} = 10^7$, $V_T = -12$ V) for films on HMDS-treated substrates. Upon annealing at 240 °C, however, the response of devices on hydrophobic substrates decreases significantly.

Crystal Structure. Molecule **19** was designed to provide insight into the intermolecular packing of this new class of **BTI**-based materials via a single-crystal structure determination. Crystals were obtained by slow sublimation under reduced pressure, and the crystal structure was determined by X-ray diffraction. Compound **19** crystallizes in a trigonal lattice belonging to the *R*-3 space group. The molecules are organized in a pseudomicellular motif with alkyl tails in the center and the conjugated cores pointing outward (Figure 14). The conjugated cores exhibit excellent $\pi-\pi$ stacking with the closest C···C distance in the direction of $\pi-\pi$ stacking being 3.43 Å (C7−C15). The *n*-hexyl tails are highly disordered beyond the third carbon atom (C21). Ring strain in the planar 7-membered ring is compensated by a slight increase in all internal bond angles, resulting in a minimal l4.6° out-of-plane imide torsion (C9−C10:C8−C11). The most significant bond angle enlargement of ~7.4° is centered at the imide nitrogen atom (C9−N1−C10) at an angle of 132.4° from a nominal angle of ~125°. Other important metrical parameters are summarized in Supporting Information Tables S1−S3.

Discussion

Molecular Modeling and Crystal Packing. Knowledge of the molecular geometry as well as the frontier molecular orbital spacial characteristics and energetics is key to understanding charge-transport efficiency, majority carrier type, and charge trapping in organic semiconductor-based devices. Moreover, the molecular geometry determines the extent of π conjugation and

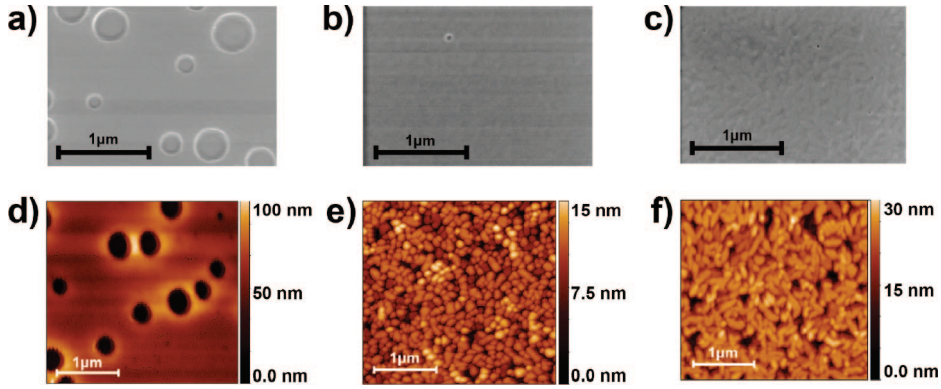

Figure 10. SEM (upper) and AFM (lower) images of **P1** films spin cast from $CHCl_3$ then annealed at 120 °C for 30 min (a, d), 240 °C for 2 h (b, e), and 300 °C for 30 min (c, f, respectively).

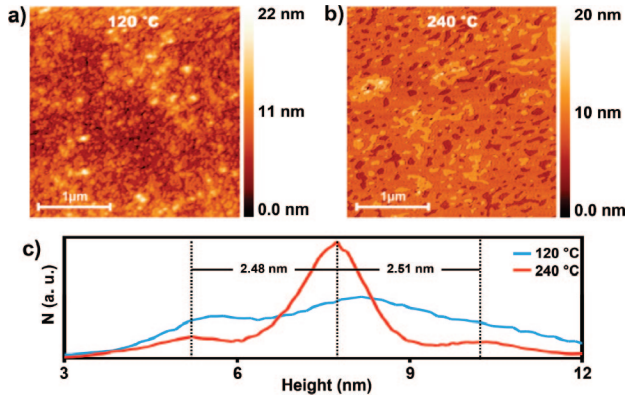

Figure 11. AFM images of **P1** films spin cast from TCB and annealed at 120 °C for 30 min (a) and 240 °C for 2 h (b), and a height histogram (c) for both images (120 °C in blue and 240 °C in red) revealing formation of a terraced surface having a 2.50 nm step height.

crystal packing, both of which directly impact intra- and interchain charge transport. Before the synthesis of any **BTI** polymers, these properties were evaluated in monomeric model structures using quantum chemical modeling, electrochemistry, optical spectroscopy, and single-crystal X-ray diffraction structure determination. The electronic structure and molecular geometry of several candidate structures was first investigated computationally using density functional theory (DFT) to determine if their properties were consistent with those required for efficient charge transport. This presynthesis theoretical study was undertaken to suggest the design of this new class of polymer semiconductors by confirming favorable molecular properties and evaluating the merit of the design choices. Since FET performance can also be influenced by phenomena that cannot be efficiently modeled at present (i.e., crystal packing, grain-boundary effects, dielectric−semiconductor interfacial interactions, and long-range film morphology), this methodology focuses on those intrinsic molecular factors required for efficient, long-range charge transport. The approach should be viewed as a means to validate favorable properties of candidate materials, evaluate structural modification options, and eliminate structures/options that have properties inconsistent with efficient charge transport. Such undesirable properties include nonplanar intramonomer geometry, significant intermonomer dihedral angles, highly localized frontier orbitals, and intrusion of functional groups in the area of $\pi-\pi$ stacking. This novel design approach is fundamentally different from previous computational studies of organic semiconductors where materials were evaluated to understand charge-transport behavior at a mechanistic level, postsynthesis.[50–52]

Five key properties of these **BTI** materials were assessed: (a) planarity of the π-conjugated portion of the monomer, (b) intermonomer dihedral angle, (c) steric effects of the functional groups, (d) frontier molecular orbital delocalization, and (e) frontier orbital energies. Geometry optimizations performed using DFT-level theory on a **BTI** trimer and a **BTI**-bithiophene-**BTI** co-oligomer reveal negligible $\pi-$core and intercore torsion (Figure 3). Such intra/intermonomer planarity is important since it allows efficient $\pi-\pi$ stacking and charge delocalization/stabilization along the π-conjugated polymer backbone. The equilibrium structures also reveal that the substituent on the imide N atoms is electronically and spatially isolated from the π orbitals. Separation from the frontier orbitals minimizes the electronic energetic effects of varying the imide substituent, limiting their influence on crystal packing and solubility. The spatial separation suggests a tolerance for sterically demanding functional groups without spatial intrusion into the $\pi-\pi$ stacking region.

The molecular orbital electron density plots reveal that the HOMO and LUMO are completely delocalized on the **BTI** trimer and co-oligomer (Figure 3b and 3c, respectively), indicating a propensity for both hole and electron stabilization. Molecular orbital energy levels were computed to predict the majority charge carrier type. The co-oligomer HOMO energy of −5.9 eV is consistent with that of polymers[14,17,18] exhibiting air-stable p-channel FET operation, while the LUMO lies somewhat higher than those of known n-channel materials.[24,50,51,53,54] In contrast, the −3.5 eV LUMO energy of the **BTI** trimer is within the energetic regime for n-channel FET materials,[15,24,50,51,54] while the HOMO lies below that of known p-channel materials. This energy level analysis suggests that **BTI** homopolymers should exhibit n-channel FET activity, while copolymers with bithiophene are better suited for p-channel behavior. Finally, the dipole moments of the **M1** and **M2** monomers are calculated to be 2.27 and 3.78 Debye, respectively. For monomers aligned antiparallel in the crystal lattice (as in the case of **19**), the

(50) Osuna, R. M.; Ortiz, R. P.; Okamoto, T.; Suzuki, Y.; Yamaguchi, S.; Hernandez, V.; Lopez Navarrete, J. T. *J. Phys. Chem. B* **2007**, *111*, 7488–7496.
(51) Hutchison, G. R.; Ratner, M. A.; Marks, T. J. *J. Am. Chem. Soc.* **2005**, *127*, 2339–2350.
(52) Oliva, M. M.; Delgado, M. C. R.; Casado, J.; Raposo, M. M. M.; Fonseca, A. M. C.; Hartmann, H.; Hernandez, V.; Navarrete, J. T. L. *Comput. Lett.* **2007**, *3*, 1–12.

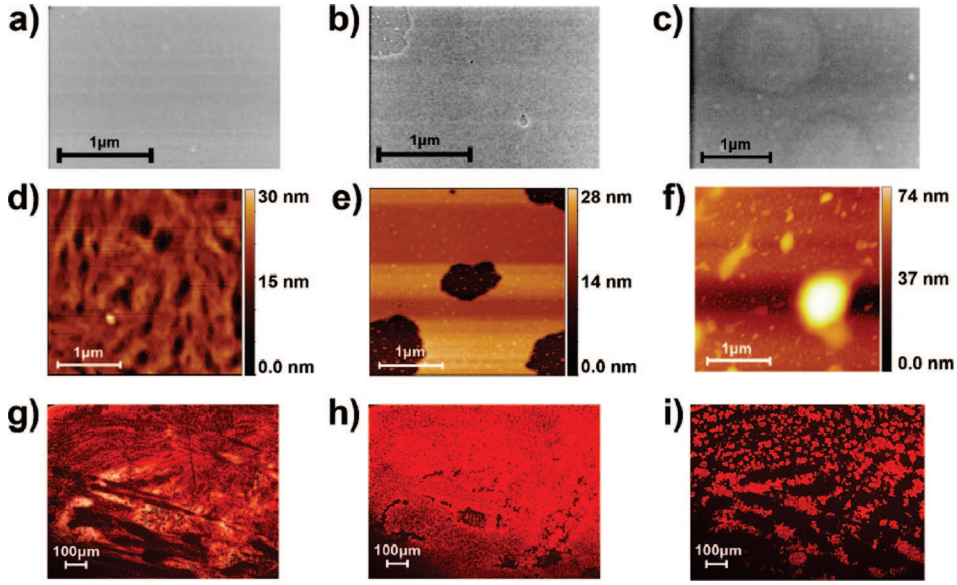

Figure 12. SEM (upper) and AFM (middle) images of **P2** films on HMDS treated substrates annealed for 30 min at 120 °C (a, d), 180 °C (b, e), and 240 °C (c, f) as well as polarized (90°) optical micrographs (lower) of **P2** on glass imaged at 120 °C (g) in the crystalline phase, 180 °C (h) as a liquid-crystal, and at 220 °C during the melting transition (i).

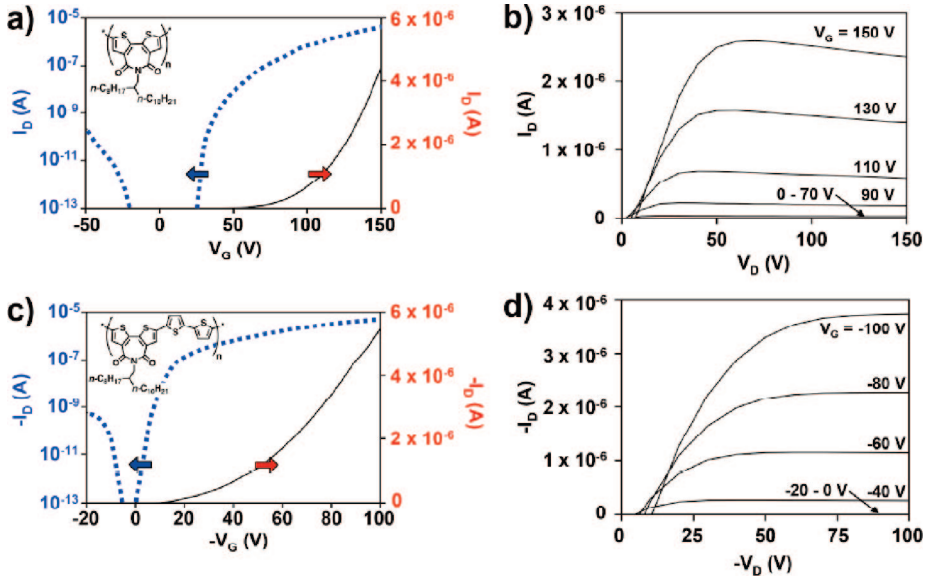

Figure 13. FET transfer (a) and output (b) plots of **P1** spin cast onto an HMDS-treated substrate and annealed at 240 °C for 2 h, and **P2** (c and d, respectively) spin cast onto an HMDS-treated substrate and annealed at 180 °C for 30 min.

Table 3. FET Performance Measured under Vacuum for Homopolymer **P1** Films Spin Cast or Drop Cast (DC) from the Indicated Solvents onto HMDS-Treated Substrates (Standard deviations are given in parentheses)

	chloroform			tetrahydrofuran			1,2,4-trichlorobenzene		
anneal[a] (°C)	μ_e (cm^2 V^{-1} s^{-1})	V_T (V)	$I_{on:off}$	μ_e (cm^2 V^{-1} s^{-1})	V_T (V)	$I_{on:off}$	μ_e (cm^2 V^{-1} s^{-1})	V_T (V)	$I_{on:off}$
120	$1.7\ (1) \times 10^{-3}$	77 (6)	$4\ (4) \times 10^{6}$	$5\ (2) \times 10^{-4}$	87 (6)	$2\ (1) \times 10^{6}$	$5\ (2) \times 10^{-4}$	90 (11)	$2\ (2) \times 10^{4}$
240	$7.8\ (8) \times 10^{-3}$	80 (5)	$4\ (1) \times 10^{7}$	$8\ (2) \times 10^{-4}$	80 (11)	$8\ (5) \times 10^{6}$	$5.8\ (2) \times 10^{-3}$	88 (8)	$2\ (1) \times 10^{7}$
240(2h)	$1.1\ (3) \times 10^{-2}$	75 (4)	$2\ (2) \times 10^{7}$	$6\ (1) \times 10^{-3}$	71 (3)	$2\ (2) \times 10^{7}$	$7.2\ (1) \times 10^{-3}$	78 (1)	$2\ (1) \times 10^{7}$
300	$1.8\ (1) \times 10^{-4}$	95 (2)	$2\ (1) \times 10^{3}$	$8\ (2) \times 10^{-5}$	93 (1)	$3\ (1) \times 10^{5}$	$1.7\ (4) \times 10^{-5}$	115 (2)	$5\ (1) \times 10^{1}$
DC	$3.2\ (5) \times 10^{-3}$	70 (7)	$2\ (1) \times 10^{7}$				$6\ (3) \times 10^{-4}$	60 (32)	$2\ (3) \times 10^{6}$

[a] Films annealed for 30 min unless otherwise noted.

magnitude of the dipole moment can be used to estimate the gas-phase dipole−dipole interaction energy using eq 1.[55]

$$V = \frac{\vec{\mu}_1 \vec{\mu}_2}{4\pi\epsilon_0 r^3} \qquad (1)$$

Here $\vec{\mu}_1$ and $\vec{\mu}_2$ are the dipole moment vectors of the monomers, ϵ_0 is the vacuum permittivity, and the distance between the dipoles r is taken to be 3.43 Å, the cofacial stacking distance observed in the crystal structure of **19**. The dipole−dipole interaction is estimated to be −1.84 kcal/mol for **M1**, which,

Table 4. FET Performance Values Measured under Vacuum and Air for Copolymer **P2** Films Spin Cast or Drop Cast (DC) from 1,2-Dichlorobenzene onto Either HMDS-Treated or Untreated SiO_2 Substrates (Standard deviations are given in parentheses)

		HMDS			SiO_2		
	anneal[a] (°C)	μ_h ($cm^2\ V^{-1}\ s^{-1}$)	V_T (V)	$I_{on:off}$	μ_h ($cm^2\ V^{-1}\ s^{-1}$)	V_T (V)	$I_{on:off}$
vacuum	120	$6\ (1) \times 10^{-3}$	−28 (2)	$9\ (8) \times 10^{6}$	$4\ (1) \times 10^{-6}$	−34 (4)	$1\ (1) \times 10^{4}$
	180	$8\ (2) \times 10^{-3}$	−12 (7)	$2\ (3) \times 10^{7}$	$2\ (1) \times 10^{-5}$	−11 (1)	$3\ (4) \times 10^{4}$
	240	$3\ (2) \times 10^{-5}$	−70 (15)	$7\ (3) \times 10^{3}$	$9\ (1) \times 10^{-6}$	−4 (5)	$5\ (3) \times 10^{3}$
	DC	$4\ (3) \times 10^{-3}$	−27 (13)	$6\ (5) \times 10^{6}$	$2\ (1) \times 10^{-5}$	−18 (2)	$7\ (6) \times 10^{4}$
air[b]	120	$4\ (1) \times 10^{-3}$	−40 (6)	$1\ (1) \times 10^{7}$	$3\ (2) \times 10^{-6}$	−33 (7)	$2\ (1) \times 10^{4}$
	180	$6\ (1) \times 10^{-3}$	−18 (4)	$1\ (2) \times 10^{7}$	$2\ (1) \times 10^{-5}$	−26 (17)	$3\ (3) \times 10^{4}$
	240	$7\ (1) \times 10^{-6}$	−82 (4)	$3\ (2) \times 10^{3}$	$6\ (1) \times 10^{-6}$	−1 (3)	$6\ (1) \times 10^{4}$
	DC	$2\ (1) \times 10^{-3}$	−40 (6)	$8\ (1) \times 10^{6}$	$2\ (1) \times 10^{-5}$	−34 (21)	$7\ (3) \times 10^{4}$

[a] Films annealed for 30 min unless otherwise noted. [b] Devices measured after 1 week in air.

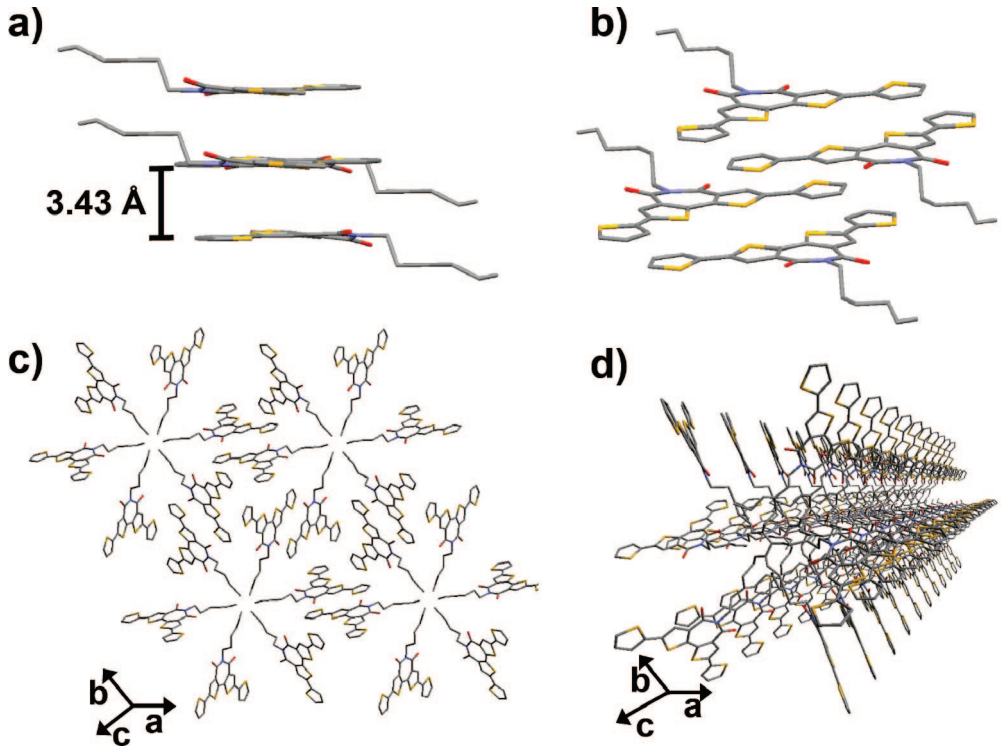

Figure 14. Crystal structure of the π-stacked **19** tetramer (a, b) and views along the *c* axis (c, d) displayed without hydrogen atoms and with only one *n*-hexyl group orientation for clarity. Carbon atoms are shown in gray, oxygen in red, sulfur in yellow, and nitrogen in blue.

all other things being equal, should stabilize formation of antiparallel dimers. The magnitude of this stabilization is sufficient to direct the crystal packing in **P1** but still allow solubilization under appropriate conditions. The larger dipole moment of **M2** results in a significantly stronger −5.11 kcal/mol dimer interaction energy, suggesting enhanced **P2** aggregation over **P1**. This significant increase in aggregation affinity is in accord with the diminished solubility and, hence, the lower average degree of polymerization achieved for **P2** vs **P1**. The limited degree of polymerization of these materials illustrates a primary challenge to achieving solution processable semiconductors active in n-type FETs. Additionally, overcoming the barrier to ambient atmosphere operation typically requires substitution of the aromatic core with even stronger electron-withdrawing groups, further limiting solubility and therefore polymer chain length.

Since it is difficult to obtain precise structural information about this new class of materials from polymeric samples alone, model molecular compound **19** was also synthesized. This molecule is similar to **M2** (a monomer for **P2**) except for the *n*-hexyl solubilizing group instead of the 2-branched alkyl moiety in **M2** and **P2**. The single-crystal X-ray structure of this compound (Figure 14) reveals a highly planar conjugated core with negligible torsion of the imide ring of 4.3° (C8−C7−C12−C11). The molecules assemble in tetramers packed antiparallel in a face-to-face fashion with a short $\pi-\pi$ distance of 3.43 Å. These π-stacked tetramers organize into larger micelle-like formations with the lipophilic solubilizing groups pointed inward, surrounded by the π-stacked clusters. The recent discovery of a similar secondary structure in another π-stacked semiconductor, rubrene, has sparked interest in potential uses for such unique small clusters of organic semiconductors.[56,57] Although this molecular crystal secondary structure is intriguing, it is unlikely that the target polymers can organize into an analogous

(53) Chesterfield, R. J.; Newman, C. R.; Pappenfus, T. M.; Ewbank, P. C.; Haukaas, M. H.; Mann, K. R.; Miller, L. L.; Frisbie, C. D. *Adv. Mater.* **2003**, *15*, 1278–1282.
(54) Risko, C.; Kushto, G. P.; Kafafi, Z. H.; Bredas, J. L. *J. Chem. Phys.* **2004**, *121*, 9031–9038.
(55) Atkins, P. W.; de Paula, J. *Physical Chemistry*, 7th ed.; W. H. Freeman and Co.: New York, 2002; p 1139.

micellular structure due to the order induced by the longer macromolecular chain length. Nonetheless, the short-range structural information obtained from this model compound is relevant since the important dipolar, steric, and $\pi-\pi$ stacking forces that determine monomer−monomer packing are reasonably conserved in the polymers.

There is also significant free volume in the crystal lattice of **19** for conformational mobility of the alkyl solubilizing groups as evidenced by the observed disorder of the *n*-hexyl substituent beyond the third carbon atom (C21). As predicted, the intermolecular antiparallel imide orientation forces the solubilizing groups to opposite sides of π-stacked polymer chains, minimizing steric crowding from adjacent chains, which could impede intermolecular core stacking. In combination with computational results on branched alkanes, these findings suggest that it should be possible to maintain optimal polymer chain geometry and favorable $\pi-\pi$ stacking even when sterically demanding solubilizing groups are introduced. Importantly, these poly(**BTI**s) should exhibit significant solubilizing group tolerance while concurrently optimizing the synthesis, solubility, solution rheology, crystallinity, and device performance.

Optical absorption spectroscopic data for polymers **P1** and **P2** as well as for monomers **M1** and **M2** reveal informative optical properties when thiophenes are incorporated into the **BTI** framework (Figure 6 and Table 1). Absorbtion maxima (λ_{max}) in solution exhibit a bathochromic shift as conjugation length is increased from **M1** to **M2** to the corresponding homo/copolymers with vibronic features significantly more pronounced in the polymers. There are minimal differences between the solution and thin-film absorption spectra of either **M1** or **P1**, while the compounds with electron-rich unfunctionalized thiophenes exhibit significant bathochromic shifts of 23 nm for **M2** and 98 nm for **P2**. This suggests that the excited states of the thiophene-substituted molecule and copolymer are better stabilized in the solid state than in solution, possibly by bithiophene−bithiopheneimide charge transfer.[58,59] The 9 nm hypsochromic shift observed in **P1** films indicates slight destabilization of S_1 in the solid state, likely a result of the highly antiparallel ground-state dipole arrangement in the crystal lattice and absence of donor−acceptor-stabilized charge separation.[60] Finally, enhanced bathochromic vibronic features in the **P2** films reflect the observed high degree of structural order of this material in the solid state.[58,61]

The redox properties of the present polymers were studied by cyclic voltammetry to investigate frontier MO energetics. Reversible reduction events are observed for all materials in this study with the polymers exhibiting multiple reversible reductions (Figure 7 and Table 2). **P1** exhibits the most pronounced reduction events with half-wave potentials at −1.11 and −1.32 V vs SCE, while the reductions for copolymer **P2** occur at −1.34 and −1.54 V. Previous work has shown that materials with reduction potentials greater than or equal to ca. −1.2 V vs SCE can exhibit efficient electron transport while those that are more difficult to reduce tend not to be active in conventional top-contact n-channel FETs.[24,36] It has been

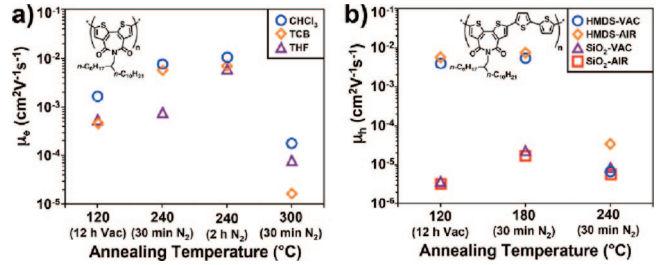

Figure 15. Plots of measured FET charge carrier mobility versus annealing temperature for **P1** films on HMDS-treated substrates measured under vacuum for the indicated spin-coating solvents (a) and **P2** films on untreated or HMDS-treated substrates measured under vacuum and air (b).

postulated that this phenomenon is caused by trapping of mobile electrons by dielectric surface hydroxyl groups, which is avoided by decreasing the LUMO energy to provide sufficient charge carrier stabilization. Recent results also suggest that the reduction potential of **P1**, −1.11 V, is likely insufficient for n-channel FET operation in air.[62] Conversely, oxidation of copolymer **P2** is 0.23 V easier at +1.48 V than is that of the homopolymer at +1.71 V. Oxidation potentials in this range are typical for polymers such as F8T2 ($E_{ox}^{1/2}$ = +1.4 V) used in air-stable p-channel FETs.[1,14,17,18,63] These electrochemical data and the favorable crystal geometry suggest that homopolymer **P1** should exhibit electron transport under inert atmosphere, while the copolymer **P2** is better suited for hole transport. The suppositions are found to be correct.

Polymer Thin-Film Morphology and Field-Effect Transistor Device Optimization. The FET performance of the polymers synthesized in this study is strongly correlated with the surface chemical functionalization and energy of the gate dielectric/substrate onto which they are cast. Thus, **P1** films on hydrophobic HMDS-treated substrates exhibit outstanding n-channel FET performance, while those cast on untreated hydrophilic SiO_2 do not exhibit FET activity. Similarly, copolymer **P2** exhibits enhanced p-channel FET performance when cast on HMDS-treated versus untreated substrates. To understand this variation in FET performance and the influence of casting solvent and annealing conditions (Figure 15), AFM, SEM, and WAXRD are used to understand polymer film surface and microstructure.

Films of homopolymer **P1** were cast from three different solvents ($CHCl_3$, THF, and TCB) and then annealed at various temperatures (120, 240, and 300 °C) to evaluate the effects on surface morphology, roughness, film crystallinity, and most importantly FET response. As seen in Table 3 and Figure 15, n-channel FET performance after the 120 °C annealing process is a function of the casting solvent with films from $CHCl_3$ solutions having the highest μ_e (1.7×10^{-3} cm^2 V^{-1} s^{-1}) and films from THF and TCB having slightly lower μ_e (5×10^{-4} cm^2 V^{-1} s^{-1}) and $I_{on:off}$ with a higher V_T. Interestingly, n-channel FET performance becomes less dependent on casting solvent when films are annealed at 240 °C for 2 h. Under these conditions μ_e of all films converges to $\sim 10^{-2}$ cm^2 V^{-1} s^{-1} with V_T values of ~75 V and $I_{on:off} > 10^7$. The relatively large V_T for all **P1**-based devices is likely a result of charge trapping in the semiconductor or at the semiconductor−dielectric interface.

(56) Blum, M.-C.; Cavar, E.; Pivetta, M.; Patthey, F.; Schneider, W.-D. *Angew. Chem., Int. Ed.* **2005**, *44*, 5334–5337.
(57) Perez-Garcia, L. A.; David, B. *Chem. Soc. Rev.* **2007**, *36*, 941–967.
(58) Choi, D. S.; Huang, S.; Huang, M.; Barnard, T. S.; Adams, R. D.; Seminario, J. M.; Tour, J. M. *J. Org. Chem.* **1998**, *63*, 2646–2655.
(59) Khan, M. N. *J. Chem. Soc., Perkin Trans. 2* **1987**, 819.
(60) Orti, E.; Viruela, P. M.; Viruela, R.; Effenberger, F.; Hernandez, V.; LopezNavarrete, J. T. *J. Phys. Chem. A* **2005**, *109*, 8724–8731.
(61) Baldwin, J. E. *J. Chem. Soc., Chem. Commun.* **1976**, 734.
(62) Jones, B. A.; Facchetti, A.; Marks, T. J.; Wasielewski, M. R. *Chem. Mater.* **2007**, *19*, 2703–2705.
(63) Oar, M. A.; Marks, T. J.; Facchetti, A. *Abstr. Pap. Am. Chem. Soc.* **2003**, *225*, U514−U514.

Since crystallinity is an important parameter in FET performance,[64] WAXRD $\theta-2\theta$ diffraction data were used to evaluate film crystallinity in all samples. The resulting diffraction patterns indicate that films of **P1** cast onto untreated hydrophilic substrates have poor crystallinity even after annealing with only broad first- and second-order Bragg peaks (Supporting Information Figures S1 and S2). This explains the lack of FET activity in these films since crystallinity is typically a critical property for efficient charge transport.[35,65–67] In marked contrast, films cast onto HMDS-treated substrates exhibit pronounced diffraction features that generally increase with annealing temperature and duration. A single family of Bragg peaks (up to fifth order) is observed in all samples, revealing an extreme degree of crystallinity versus typical polymer films (Figure 8).[65,66] Laue fringes at $2\theta < 4°$ observed in some $\theta-2\theta$ patterns of films cast from TBC evidence very smooth and highly uniform films.[68,69] The increase in crystallinity corresponds well with the n-channel FET performance enhancement observed as the film samples are annealed with the exception of those annealed $\geq$300 °C. Diminished FET response is observed in these samples even though the crystallinity continues to increase. This fall in performance is likely not a result of chemical decomposition since the materials are stable to ~400 °C as determined by TGA (Figure 5a at a ramp rate of 5 °C/min) but rather can be explained by changes in the film morphology as revealed in AFM and SEM images.

Although WAXRD is a powerful tool that probes overall film crystallinity, other crucial properties such as film uniformity and crystallite connectivity affect transistor performance. AFM and SEM images show that films cast from the low-boiling solvents exhibit irregular morphologies characterized by the circular voids as observed in Figure 10 for $CHCl_3$-cast films and in Supporting Information Figure S4 for THF-cast films. These irregularities disappear when the samples are annealed at 240 and 300 °C, resulting in more continuous films. For example, the rms roughness of $CHCl_3$-cast films decreases from 17 nm when annealed at 120 °C to a smoother and more continuous polycrystalline surface having 2.6 nm rms roughness when annealed at 240 °C for 2 h. However, the surface rms roughness of all samples increases by 2−12 nm when the film annealing is performed at 300 °C, and imaging shows the emergence of individual crystallites. This observation suggests that the polymer begins to undergo aggregation into larger, discrete domains that are not well interconnected.[70] Such a decrease in crystallite connectivity would impede charge hopping, resulting in lower observed FET mobility.[49,71]

A unique feature discovered in **P1** films cast from TCB is terracing (Figure 11), a phenomenon typically observed in highly ordered polymers, such as poly(ethylene terephthalate),[72] poly(2-(perfluorooctyl)ethyl acrylate),[73] block copolymers,[74,75] and polyhydroxyalkanoates.[76] It is rarely observed in organic semiconducting materials and then only in highly crystalline molecular semiconductors.[77–79] Recently, terracing was observed in a semiconducting polymer by annealing p-channel poly(2,5-bis(3-hexadecylthiophene-2-yl)thieno[3,2-*b*]thiophene) in the liquid crystalline phase, revealing a step height matching the WAXRD-derived *d* spacing.[21,49] AMF images of annealed **P1** films cast from TCB exhibit a highly terraced surface having step heights of 2.50 nm, which can be accurately determined from the trimodal distribution of the AFM height histogram (Figure 11c). This height is in good agreement with the 25.2 Å *d* spacing determined by WAXRD, which corresponds to the height of a polymer layer tilted at an angle of ~69.0° relative to the substrate plane (assuming negligible side chain interdigitation). This rare terraced structure emphasizes the exceptional degree of crystallinity that **P1** films can attain.

Copolymer **P2** exhibits air-stable p-channel FET performance that is a marked function of substrate surface energy and annealing temperature. Annealing temperatures of 120, 180, and 240 °C were chosen to correspond to the phase transitions observed in the DSC traces (Figure 5). FET performance on HMDS-treated substrates initially increases from $\mu_h = 6 \times 10^{-3}$ $cm^2\ V^{-1}\ s^{-1}$ when annealed at 120 °C to 8×10^{-3} $cm^2\ V^{-1}\ s^{-1}$ when annealed at 180 °C before declining precipitously with 240 °C annealing (Table 4 and Figure 15). The performance of devices fabricated on untreated hydrophilic substrates also exhibits a similar annealing trend, although hole mobilities are 2 orders of magnitude lower. These p-channel FETs were originally characterized under high vacuum and then again after exposure to air for 1 week, exhibiting no change in $I_{on:off}$, a 5−10 V increase in V_T, and only a 20% decrease in hole mobility.

As in the case of the homopolymer, WAXRD reveals that **P2** films deposited on HMDS-treated substrates have significantly greater crystallinity than those on untreated SiO_2. The reflection intensities increase and peak widths decrease when **P2** films on hydrophobic substrates are annealed at 180 and 240 °C, while those on untreated substrates exhibit only moderately increased intensities. These observations demonstrate the enhanced crystallinity achieved with annealing and correlate with greater hole mobilities for films annealed at 180 °C. Interestingly, although the WAXRD of **P2** films on hydrophobic substrates annealed at 300 °C indicates very substantial crystallinity, the μ_h in these films decreases markedly.

Surface characterization with AFM and SEM provides additional understanding of the observed performance trends of **P2**-based FETs. Films cast on untreated SiO_2 substrates have an initial rms roughness of 1.2 nm that increases only slightly

(64) DeLongchamp, D. M.; Kline, R. J.; Lin, E. K.; Fischer, D. A.; Richter, L. J.; Lucas, L. A.; Heeney, M.; McCulloch, I.; Northrup, J. E. *Adv. Mater.* **2007**, *19*, 833–837.
(65) Chang, P. C.; Lee, J.; Huang, D.; Subramanian, V.; Murphy, A. R.; Frechet, J. M. J. *Chem. Mater.* **2004**, *16*, 4783–4789.
(66) Kline, R. J.; McGehee, M. D.; Kadnikova, E. N.; Liu, J. S.; Frechet, J. M. J.; Toney, M. F. *Macromolecules* **2005**, *38*, 3312–3319.
(67) Knipp, D.; Street, R. A.; Volkel, A. R. *Appl. Phys. Lett.* **2003**, *82*, 3907–3909.
(68) Durr, A. C.; Schreiber, F.; Munch, M.; Karl, N.; Krause, B.; Kruppa, V.; Dosch, H. *Appl. Phys. Lett.* **2002**, *81*, 2276–2278.
(69) Moulin, J. F.; Dinelli, F.; Massi, M.; Albonetti, C.; Kshirsagar, R.; Biscarini, F. *Nucl. Instrum. Methods Phys. Res.* **2006**, *246*, 122–126.
(70) Azumi, R.; Gotz, G.; Debaerdemaeker, T.; Bäuerle, P. *Chem.-Eur. J.* **2000**, *6*, 735–744.
(71) Joseph, K. R.; McGehee, M. D.; Toney, M. F. *Nat. Mater.* **2006**, *5*, 222–228.
(72) Sakai, Y.; Imai, M.; Kaji, K.; Tsuji, M. *J. Cryst. Growth* **1999**, *203*, 244–254.
(73) Kim, J.; Efimenko, K.; Genzer, J.; Carbonell, R. G. *Macromolecules* **2007**, *40*, 588–597.
(74) Tsarkova, L.; Knoll, A.; Krausch, G.; Magerle, R. *Macromolecules* **2006**, *39*, 3608–3615.
(75) Carvalho, B. L.; Thomas, E. L. *Phys. Rev. Lett.* **1994**, *73*, 3321.
(76) Xu, J.; Guo, B.-H.; Chen, G.-Q.; Zhang, Z.-M. *J. Polym. Sci., Part B: Polym. Phys.* **2003**, *41*, 2128–2134.
(77) Fujikake, H.; Suzuki, T.; Murashige, T.; Sato, F. *Liq. Cryst.* **2006**, *33*, 1051–1057.
(78) Chesterfield, R. J.; McKeen, J. C.; Newman, C. R.; Ewbank, P. C.; da Silva, D. A.; Bredas, J. L.; Miller, L. L.; Mann, K. R.; Frisbie, C. D. *J. Phys. Chem. B* **2004**, *108*, 19281–19292.
(79) Fujikake, H.; Suzuki, T.; Murashige, T.; Sato, F. *Liq. Cryst.* **2006**, *33*, 1051–1057.

to 1.4 nm with annealing at 240 °C. Correspondingly, device performance and WAXRD diffraction patterns of films on these bare SiO_2 samples exhibit only modest changes with annealing. In contrast, the surface of **P2** on HMDS-treated substrates changes dramatically from a continuous film having a 4 nm surface rms roughness when annealed at 120 °C to a substantially delaminated film on annealing at 240 °C. This film dewetting is observed in the SEM images as polymer droplets (Figure 12f) and in the AFM images as increased roughness and formation of the large islands in Figure 12c. Films annealed at 180 °C exhibit very smooth surfaces having an rms roughness of 1.3 nm (excluding voids), although ~1 μm voids revealed by both AFM and SEM imaging indicate initial dewetting. Cross-polarized optical microscopy of **P2** films cast on untreated glass reveals that at 180 °C (Figure 12h) **P2** has undergone a liquid-crystalline transition at 127 °C but has not yet melted. Annealing above the 196 °C **P2** melting temperature (see image of the melting transition, Figure 12i) is accompanied by complete dewetting of films on hydrophobic surfaces, resulting in significant diminution in p-channel FET performance for the 240 °C anneal.[80]

Conclusions

This work demonstrates a novel approach to organic semiconductor development, where presynthesis computational modeling guides materials design from initial conception to refinement of the final semiconductor structure. Through computational understanding of molecular geometry as well as frontier orbital symmetry and energetics, the novel building block 2,2′-bithiophene-3,3′-dicarboximide is identified. Properties predicted by this modeling are confirmed by the crystal structure of the model molecule **19**, which reveals $\pi-$core planarity, antiparallel **BTI** packing, a short cofacial $\pi-\pi$ distance of 3.43 Å, and a favorable solubilizing group orientation. From the synthesis of a series of 10 homo/copolymers, two materials were identified as having favorable solubility and solution rheology in common organic solvents. Polymer films exhibit extremely high crystallinity with **P1** displaying exceptional n-channel FET performance ($\mu_e = 0.011 \pm 0.003$ cm^2 V^{-1} s^{-1}, $I_{on:off} > 10^7$) and **P2** air-stable p-channel FET operation ($\mu_h = 0.008 \pm 0.002$ cm^2 V^{-1} s^{-1}, $I_{on:off} = 10^7$). While the behavior of many high-performance semiconductors is sensitive to deposition conditions, **BTI** polymer films exhibit FET performance predominately independent of film-casting conditions. The extraordinary degree of thin-film order in **BTI**-based materials is also revealed by topographical terracing of the annealed **P1** films, a phenomenon observed only once previously for a polymer semiconductor. The excellent figures of merit of this new class of polymeric semiconductors reveals the efficacy of the present novel and general computationally aided materials design strategy, employed here for the first time in organic electronic materials.

Acknowledgment. We thank the NSF-MRSEC (DMR-0520513) and ONR (N00014-05-10766) for support of this research. We also thank Prof. R. Jordan and Dr. E. Szuromi of the University of Chicago for hospitality with the HT-GPC characterization.

Supporting Information Available: Full surface microstructure characterization (SEM, AFM, XRD) data, CIF file, and complete refs 2e and 43. This material is available free of charge via the Internet at http://pubs.acs.org.

JA710815A

(80) Yiliang, W.; Ping, L.; Beng, S. O.; Tharan, S.; Ni, Z.; Gianluigi, B.; Shiping, Z. *Appl. Phys. Lett.* **2005**, *86*, 142102.